WILEY

Research Article

Damage Identification in Large-Scale Bridge Girders Using Output-Only Modal Flexibility–Based Deflections and Span-Similar Virtual Beam Models

N. T. Le ⓘ,[1] A. Nguyen ⓘ,[2] T. H. T. Chan ⓘ,[3] and D. P. Thambiratnam ⓘ[3]

[1]*Faculty of Hydraulic Engineering, Hanoi University of Civil Engineering, Hanoi, Vietnam*
[2]*School of Engineering, University of Southern Queensland, Toowoomba, Australia*
[3]*School of Civil & Environmental Engineering, Queensland University of Technology, Brisbane, Australia*

Correspondence should be addressed to A. Nguyen; andy.nguyen@unisq.edu.au

Damage identification (DI) methods using changes in static and modal flexibility (MF)–based deflections are effective tools to assess the damage in beam-like structures due to the explicit relationships between deflection change and stiffness reduction caused by damage. However, current methods developed for statically determinate beams require the calculation of mathematical scalar functions which do not exist in statically indeterminate beams and limit their application mainly to single-span bridges and cantilever structures. This paper presents an enhanced deflection-based damage identification (DBDI) method that can be applied to both statically determinate and indeterminate beams, including multispan girder bridges. The proposed method utilises the deflections obtained either from static tests or proportional deflections extracted from output-only vibration tests. Specifically, general mathematical relationships between deflection change and relative deflection change with respect to the damage characteristics are established. From these, additional damage-locating criteria are proposed to help distinguish undamaged spans from the damaged ones and to identify the damage location within the damaged span. Notably, a span-similar virtual beam (SSVB) model concept is introduced to quantify the damage and make this task straightforward without the need to calculate complicated mathematical formulae. This model only requires information of the beam span length, which can be conveniently and accurately obtained from a real structure. The robustness of the method is tested through a series of case studies from a numerical two-span beam to a benchmark real slab-on-girder bridge as well as a complex large-scale box girder bridge (BGB). The results of these studies, including the minimal verification errors within five percent observed in the real bridge scenario, demonstrate that the proposed method is robust and can serve as a practical tool for structural health monitoring (SHM) of important highway bridges.

Keywords: damage identification; modal flexibility–based proportional deflection; output-only; span-similar virtual beam; static deflection; structural health monitoring

1. Introduction

Structural health monitoring (SHM) is an essential part of structural safety management programs to safeguard important civil engineering structures. Damage identification (DI) forms the core of SHM systems which aims to detect the onset of damage and enable proactive maintenance measures before the damage escalates and compromises the

structure's functionality [1, 2]. The fundamental principle of DI methods lies in the fact that structural damage induces detectable alterations in the structural responses. Therefore, by measuring these changes, one can assess the damage with respect to its presence, location and severity [3]. Deflection-based damage identification (DBDI) methods utilising changes in flexural deflections are viable techniques for these purposes owing to the explicit relationship between

deflection change and stiffness reduction due to damage [4, 5]. The research on DBDI methods has received considerable attention as evident from various methods developed and studied utilising either the static deflections obtained from static load tests [4, 6–18] or pseudo-deflections [19–25] and proportional deflections [26, 27] estimated from modal flexibility (MF) matrices resulted from vibration tests.

DBDI methods traditionally utilise static deflections acquired through static load testing. Within this approach, existing methods are frequently incorporated with iterative optimisation techniques to compute the damage parameters. Sanayei and Onipede [6] introduced an iterative algorithm to determine structural element stiffness changes by comparing analytical and measured static displacements under known static loads. Similarly, Banan, Banan and Hjelmstad [7, 8] utilised constrained least-square minimisation method to minimise the discrepancy between the measured displacement and that from a finite element (FE) model. Further developments include algorithms by Sanayei et al. [10] and Wang et al. [11] that incorporate static deflection and other structural responses such as static strain and natural frequencies for damage detection and severity estimation. Other approaches, such as those by Bakhtiari-Nejad, Rahai and Esfandiari [12] and Chen, Hong-Ping and Chuan-Yao [13], utilised optimisation techniques and the changes in load vectors or displacement curvatures to locate and quantify damage. Yang and Sun [14] presented a static-based damage localisation and quantification approach using the flexibility disassembly technique and a damage localisation vector derived from the static response equation. Kourehli et al. [15] applied simulated annealing algorithms to solve objective functions formulated from modal data and static displacements to locate and quantify damage in beam and frame structures. Grandić and Grandić [16] addressed the sparsity of static measurement to locate and quantify damage in simply supported beams incorporating the grey relational coefficient and curvature of displacement influence line.

By incorporating with an iterative or optimisation algorithm, above methods succeeded in both locating and quantifying damage. Without the aid of these techniques, some methods experienced difficulties in estimating the damage extend. Choi et al. [17] developed a damage locating method utilising the ratio of bending moment to the flexural rigidity. However, the applicability was limited only to specific beam types and single damage scenarios. Another method leverages changes in displacement curvature and a grey relational coefficient to identify damage location [18]. However, it lacks a direct relationship between the coefficient and damage severity, hindering quantification capability. In addressing this limitation, Le et al. [4] proposed a DBDI method that stands out for its ability to directly locate and quantify damage from measured deflection changes without optimisation or a refined FE model. This method leverages mathematical relationships between deflection changes and damage characteristics, offering a physical way to locate and quantify damage in closed-form solutions. However, it requires calculations of specific mathematical functions valid only for certain statically determinate beam types, such as simply supported and cantilever beams.

Above traditional DBDI methods using static deflections often require controlled load test settings under one-off periodic monitoring programs. These practices can be challenging in continuous monitoring programs of in-service structures, particularly highway bridges and most vertical structures such as shear buildings. An alternative approach, constituting the second DBDI approach, leverages pseudo-deflections that are not measured but estimated indirectly from MF matrices constructed from natural frequencies and mass-normalised mode shapes obtained from vibration tests [19–25]. The basic idea behind this approach is that the column flexibility at a measured degree of freedom (DOF) is physically the static displacement vector obtained from an applied unit point load (UPL) at that DOF. Therefore, from a measured MF matrix, it is possible to estimate the MF-based deflections under arbitrary virtual point loads acting at the DOFs and their combinations. Several methods have succeeded in locating and quantifying damage in shear-dominant beam-like structures such as shear buildings based on formulae that relate the storey drifts and the damage severities [19–21]. For bending-dominant beam-like structures, such as bridge girders, most of the existing methods using MF-based deflections and their derivatives primarily focus on damage detection and localisation [22, 23]. Quantifying damage severity has proven challenging due to the absence of a clear link between changes in MF and reductions in stiffness. Le et al. [24] addressed this by extending the damage-induced deflection change formulae from their previous work [4] to a series of MF-based deflection and relative deflection changes and successfully used them to locate and quantify damage in beams. However, the method still necessitates calculating specific mathematical functions that are not valid for statically indeterminate beams.

The mass-normalised mode shapes used to construct the MF matrices are available from forced-vibration tests or can be calculated from arbitrarily scaled mode shapes from ambient modal data by using a validated FE model or performing repeated mass change testing methods [28–31]. However, for large-scale structures, obtaining well-validated FE models is not always possible, and it can be difficult to add masses to real structures, especially under operational conditions [29]. Nevertheless, in the absence of mass-normalised mode shapes, it is still possible to assess the damage by using the so-called proportional modal flexibility (PMF) matrices constructed from arbitrarily scaled mode shapes [26, 27, 32–35]. It was proven that PMF matrices maintain important damage-driven information to help identify the damage. Therefore, the proportional MF-based deflections extracted from PMF matrices can be used to assess the damage in beam-like structures.

This paper presents an enhanced deflection-based method that can locate and quantify damage in different beam-like structures, including statically determinate and indeterminate beams. The method utilises either the

changes in static deflections or output-only MF-based proportional deflections. Additional damage locating criteria compared to original methods in [4, 24] are developed to identify the damage location in multispan beams. A new damage quantification method is proposed to quantify the damage and make this task straightforward without the need to calculate complicated mathematical formulae as required in existing methods for statically determinate beams. The remainder of this paper is organised as follows. First presented is the theory on the developed method and its enhanced components for locating and quantifying damage under different scenarios. Next, comprehensive verifications and applications onto FE models, the benchmark I-40 multiple span plate-on-girder bridge and a large-scale box girder bridge (BGB) are carried out to examine the capacities of the method. The paper concludes with a summary and final remarks on the study.

2. Theory

2.1. Development of Deflection-Based Damage Locating Method for Multispan Beams

2.1.1. Beam Deflection Formulation in the Undamaged State. Consider an m-span continuous Euler–Bernoulli beam ($m \geq 1$) with constant flexural stiffness EI (Figure 1(a)). Under an arbitrary UPL acting on the beam, the deflection function for each span can be expressed according to the principle of virtual work method [36] as follows:

$$u^h(x_i, x_L) = \frac{1}{EI} \int_0^{L_i} M^h(s, x_L) m(s, x_i) \, ds, \quad i = \overline{1, m},$$

$$(1)$$

where $u^h(x_i, x_L)$ is the deflection at section x_i within the ith span ($0 \leq x_i \leq L_i$) under the UPL at x_L, $M^h(s, x_L)$ is the corresponding bending moment value of the beam at section s (Figure 1(b)), "h" stands for "healthy" or intact state and $m(s, x_i)$ is the virtual bending moment value of the ith released simply supported beam at section s under the virtual unit point load (VUPL) acting at section x_i (Figure 1(c)). The beam deflection is a second ordered function with respect to x_i as depicted in Figure 1(d). The deflection formula can now be rewritten as follows:

$$u^h(x_i, x_L) = \frac{1}{EI} u_0(x_i, x_L), \quad i = \overline{1, m},$$

$$(2)$$

where $u_0(x_i, x_L)$ is the integration term in equation (1):

$$u_0(x_i, x_L) = \int_0^{L_i} M^h(s, x_L) m(s, x_i) \, ds, \quad i = \overline{1, m}.$$

$$(3)$$

For statically determinate beams, $u_0(x_i, x_L)$ can be easily formulated and used for quantifying damage in [4, 24]. However, such formulae are not available for multispan beams since the bending moment $M^h(s, x_L)$ does not exist in closed-form solution. Therefore, it is necessary to develop an alternative to the existing formula-based method that can be applicable for multiple span beams.

2.1.2. Effect of Damage on the Bending Moment. Consider a single damage at a beam segment $a \leq x_1 \leq a + b$ on one of the beam spans (Figure 2(a)). Let α be the damage severity coefficient of the damaged element, i.e., its remaining flexural stiffness is $(1 - \alpha)$ EI. The distance a from the left support to the damage and the damage's length b are the damage locating identifiers, which means the determination of a and b will enable the damage localisation. In Figure 2, DC denotes deflection change whereas RDC refers to relative deflection change.

Different from statically determinate beams, damage on one span of multispan beams will reduce the relative stiffness of that span and will therefore lead to a redistribution of internal forces throughout the beam according to the moment distribution method [36]. In particular, the bending moment will increase in the undamaged spans and decrease in the damaged span (Figure 2(b)). The bending moment in the damaged state $M^d(x_i, x_L)$ can be presented by

$$M^d(x_i, x_L) = M^h(x_i, x_L) + \Delta M(x_i, x_L), \quad i = \overline{1, m}, \quad (4)$$

where $\Delta M(x_i, x_L)$ is the moment change due to the damage. On grouping, equation (4) can be rewritten as

$$M^d(x_i, x_L) = [1 + \zeta_M(x_i, x_L)] M^h(x_i, x_L), \quad (5)$$

where $\zeta_M(x_i, x_L)$ is the relative moment change at coordinate x_i under the UPL at x_L, or:

$$\zeta_M(x_i, x_L) = \left(\frac{\Delta M(x_i, x_L)}{M^h(x_i, x_L)} \right). \quad (6)$$

Since both $M^h(x_i, x_L)$ and $M^d(x_i, x_L)$ are independent of EI, the relative moment change $\zeta_M(x_i, x_L)$ is a function of the damage characteristics (a, b and α) and is independent of the flexural rigidity EI. As depicted in Figure 2(b), the triangular shape of both M^h and M^d on the second span (without UPL applied) leads to $\zeta_M(x_2, x_L)$ being constant for all x_2, a consequence of simple geometric operations. It follows:

$$1 + \zeta_M(x_2, x_L) = 1 + \zeta_{M_2}(x_L), \quad (7a)$$

where $\zeta_{M_2}(x_L)$ is the average value of $\zeta_M(x_2, x_L)$ among the coordinates x_2 on the second span. For the first span, where the UPL is applied, the nonlinearity of the bending moment diagrams causes $\zeta_M(x_1, x_L)$ to remain constant only for $x_1 \leq x_L$ and to vary when $x_L < x_1 < L_1$. However, given that early damage in multispan beams causes insignificant moment change $\Delta M(x_i, x_L)$ compared to the original $M^h(x_i, x_L)$, the $\zeta_M(x_i, x_L)$ values along the beam span are significantly less than 1 ($\zeta_M(x_i, x_L) \ll 1$). Consequently, the following mathematical approximation holds:

$$1 + \zeta_M(x_1, x_L) \cong 1 + \zeta_{M_1}(x_L), \quad (7b)$$

where $\zeta_{M_1}(x_L)$ represents the average value of $\zeta_M(x_1, x_L)$ among the coordinates x_1 on the first span. For a general case when the UPL is applied at any location along the beam, combining equations (7a) and (7b) leads to the following approximation:
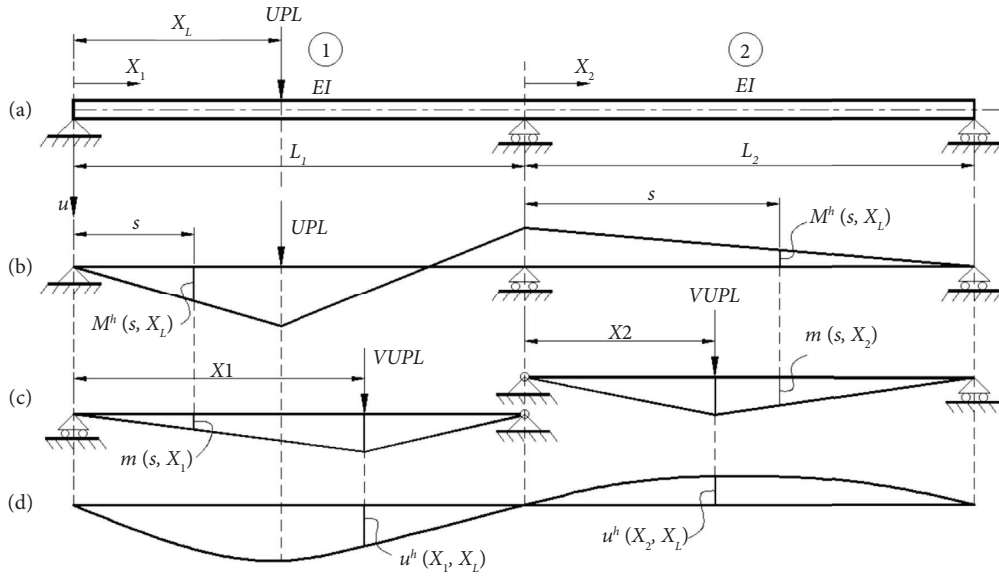
FIGURE 1: Principle of virtual work for multispan beam: (a) beam configuration; (b) bending moment diagram; (c) virtual bending moment diagrams of the released simply supported beams; (d) deflection curve.
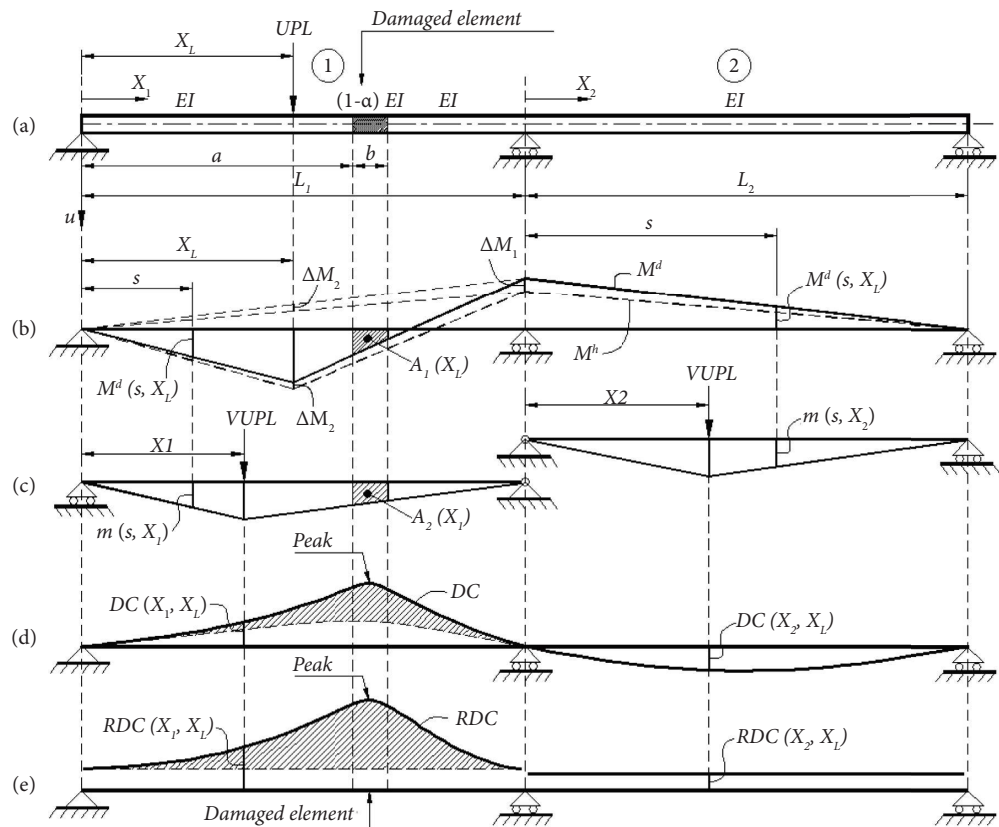
FIGURE 2: Damage-induced DC and RDC patterns: (a) beam configuration; (b) bending moment diagrams (M^h, M^d); (c) virtual bending moment diagrams of the released SS beams; (d) DC pattern; (e) RDC pattern.

$$1 + \zeta_M(x_i, x_L) \cong 1 + \zeta_{M_i}(x_L), \quad i = \overline{1, m}, \quad (8)$$

where $\zeta_{M_i}(x_L)$ represents the average value of $\zeta_M(x_i, x_L)$ among the coordinates x_i on the ith span. For illustration, a FE analysis was carried out and results are presented in the

Appendix to validate the approximation made in equation (8). Therefore, for each UPL position x_L, $\zeta_{M_i}(x_L)$ can be considered as a scalar for each beam span. On substitution of (8) into (5), an approximate relationship between the damaged and undamaged bending moment is given by

$$M^{\mathrm{d}}(x_i, x_L) \cong \left[1 + \zeta_{M_i}(x_L)\right]M^{\mathrm{h}}(x_i, x_L), \quad i = \overline{1, m}. \quad (9)$$

2.1.3. Deflection Change Pattern on the Undamaged Span Induced by Damage.

For the undamaged span (second span of Figure 2), from the principle of virtual work, the deflection function can be expressed as follows:

$$u^d(x_2, x_L) \cong \left[1 + \zeta_{M_2}(x_L)\right]\left[\frac{1}{EI}\int_0^{L_2} M^{\mathrm{h}}(s, x_L)\,m(s, x_2)\,ds\right]. \quad (11)$$

Note that the expression in the second square bracket is the undamaged deflection $u^h(x_i, x_L)$ (recall equation (1)),

$$u^d(x_2, x_L) = \int_0^{L_2}\frac{1}{EI(s)}M^{\mathrm{d}}(s, x_L)\,m(s, x_2)\,ds. \quad (10)$$

On substitution of equation (9), and noting that $EI(s) = EI = \text{constant}$ in the intact span, equation (10) is expanded and rearranged as

and the damage-induced deflection change DC and relative deflection change RDC are given by

$$\mathrm{DC}(x_2, x_L) = u^d(x_2, x_L) - u^h(x_2, x_L) \cong \zeta_{M_2}(x_L)\,u^h(x_2, x_L), \quad (12)$$

$$\mathrm{RDC}(x_2, x_L) = \left(\frac{\mathrm{DC}(x_2, x_L)}{u^h(x_2, x_L)}\right) \cong \zeta_{M_2}(x_L). \quad (13)$$

Since $\zeta_{M_2}(x_L)$ is a scalar, equation (12) reveals that the damage-induced deflection change in the undamaged span is proportional to the deflection $u^h(x_2, x_L)$, and thus it appears as a continuous curve without any abrupt changes (Figure 2(d)). Moreover, from equation (13), RDC is approximately constant in the undamaged span (Figure 2(e)). These unique patterns can be used to distinguish the undamaged spans from the damaged one in multiple span beams.

2.1.4. Deflection Change Pattern on the Damaged Span Induced by Damage.

Now consider the damaged span, i.e., the first span in Figure 2, and the deflection formula can be expressed as follows according to the principle of virtual work:

$$u^d(x_1, x_L) = \int_0^{L_1}\frac{1}{EI(s)}M^{\mathrm{d}}(s, x_L)\,m(s, x_1)\,ds. \quad (14)$$

By separating the damaged segment $[a, a+b]$, the deflection function is transformed to

$$u^d(x_1, x_L) = \frac{1}{EI}\int_0^{L_1} M^{\mathrm{d}}(s, x_L)\,m(s, x_1)\,ds + \left(\frac{1}{(1-\alpha)EI} - \frac{1}{EI}\right)\int_a^{a+b} M^{\mathrm{d}}(s, x_L)\,m(s, x_1)\,ds$$

$$= \frac{1}{EI}\int_0^{L_1} M^{\mathrm{d}}(s, x_L)\,m(s, x_1)\,ds + \frac{\alpha}{(1-\alpha)EI}\int_a^{a+b} M^{\mathrm{d}}(s, x_L)\,m(s, x_1)\,ds. \quad (15)$$

Let β be a derivative (i.e., in the sense of a variant) of the damage severity, defined by the following equation:

$$\beta = \frac{\alpha}{1-\alpha}. \quad (16)$$

As proven in [4, 24], using β as a damage severity derivative offers a convenient way for characterising the damage information from damage-induced deflection changes. On substitution of equations (9) and (1), the deflection function in the damaged span is given by

$$u^d(x_1, x_L) \cong \left[1 + \zeta_{M_1}(x_L)\right]u^h(x_1, x_L) + \frac{\beta}{EI}\int_a^{a+b} M^{\mathrm{d}}(s, x_L)\,m(s, x_1)\,ds. \quad (17)$$

Let $g(x_1, x_L)$ be the integration term in the above equation so that:

$$g(x_1, x_L) = \int_a^{a+b} M^{\mathrm{d}}(s, x_L) m(s, x_1) ds. \tag{18}$$

Equation (18) indicates that $g(x_1, x_L)$ is the volume integral of the two trapezoids areas $A_1(x_L)$ and $A_2(x_1)$, which are parts of the bending moment diagrams M^{d} and m within the damaged segment $[a, a+b]$ as depicted in Figures 2(b) and 2(c). It can be inferred from Figure 2(c) that

$A_2(x_1)$ area is maximum when $x_1 \in [a, a+b]$. Therefore, $g(x_1, x_L)$ is a peak-like function with respect to x_1, and the peak is at the damaged element $[a, a+b]$. Similarly, from Figure 2(b), $A_1(x_L)$ area is maximum when $x_L \in [a, a+b]$. Therefore, the peak's magnitude of $g(x_1, x_L)$ is higher when the UPL is applied closer to the damaged element $[a, a+b]$.

From equations (2), (17) and (18), the damage-induced deflection change DC and relative deflection change RDC on the damaged span are given by

$$DC(x_1, x_L) = u^d(x_1, x_L) - u^h(x_1, x_L) \cong \zeta_{M_1}(x_L) u^h(x_1, x_L) + \beta \frac{1}{EI} g(x_1, x_L), \tag{19}$$

$$RDC(x_1, x_L) = \left(\frac{DC(x_1, x_L)}{u^h(x_1, x_L)} \right) \cong \zeta_{M_1}(x_L) + \beta \left(\frac{g(x_1, x_L)}{u_0(x_1, x_L)} \right). \tag{20}$$

Compared to formulae in equations (12) and (13) for the undamaged span, the DC and RDC formulae in equations (19) and (20) for the damaged span comprise of an additional peak-like function, which inherit the $g(x_1, x_L)$ patterns described above. The additional parts are highlighted in Figures 2(d) and 2(e). Consequently, the $DC(x_1, x_L)$ and $RDC(x_1, x_L)$ in the damaged span are peak-like functions with respect to x_1, and the peak's magnitudes at the damaged segment are higher when the UPL is applied closer to the damaged element $[a, a+b]$ (Figures 2(d) and 2(e)). These distinctive damage-induced patterns can be used to help identify the damaged span and the damaged location in multiple span beams.

It should be noted that the above damage-induced DC and RDC patterns for the damaged span are similar to the damage-locating criteria for statically determinate beams reported in previous research [4, 24]. However, the DC and RDC functions in previous research are special cases of equations (19) and (20) on which $\zeta_{M_2}(x_L) = 0$ (since the M^h and M^d are the same), and the two scalar functions $g(x_1, x_L)$ and $u_0(x_1, x_L)$ exist in closed-form solutions. By contrast, the DC and RDC forms developed in this paper are general and applicable for both statically determinate and statically indeterminate beams.

2.1.5. The Proposed Damage Locating Concept for Multispan Beams.
From the above development, it is evidenced that both DC and RDC plots provide distinctive damage-induced patterns that can reveal the damaged span and damaged element in continuous beams based on the following multiple damage locating criteria:

1. The DC plots on the undamaged span emerge in continuous curves without any abrupt changes. This results in approximately constant RDC plots on the undamaged span.

2. By contrast, both DC and RDC plots are peak-like functions on the damaged span, with a peak at the

damaged element. This feature helps to locate the damaged element within the damaged span.

3. The magnitudes of the 'peak' of the DC and RDC plots are larger when the UPLs are closer to the damage location and largest when the UPL is applied at the damaged element. This characteristic can help to navigate the inspection load towards the damage location for more accurate detection results.

The first criterion serves as an additional damage locating indicator for identifying undamaged spans in multispan beams. The latter two criteria, which are based on the new general mathematical relationships developed in previous sections, resemble the damage locating concepts presented in [4, 24] but are applicable to both statically determinate and indeterminate beam types.

As will be illustrated in subsequent numerical and experimental verifications, the proposed damage locating method initially identifies potential damage location at peak regions of a single DC or RDC plot, guided by the first and second criteria. The identified damage location is then refined and confirmed by systematically scanning other DC and RDC plots under various UPL positions, applying the third damage locating criterion.

2.2. Development of Damage Quantification Method for Multispan Beams.
Once the damage element is identified using the method outlined in the previous section, the next step is to quantify the severity of the damage. Since the moment change magnitude due to damage is proportional to the damage severity, the relative bending moment change $\zeta_{M_i}(x_L)$ can be expressed as follows:

$$\zeta_{M_i}(x_L) = \beta \zeta_{M_i}^{50\%}(x_L), \quad i = \overline{1, m}, \tag{21}$$

where $\zeta_{M_i}^{50\%}$ is a referenced relative moment change of the beam in a virtual damage state having $\beta = 1$. From equation (16), $\beta = 1$ when $\alpha = 50\%$, which explains the notation $\zeta_{M_i}^{50\%}$ and its superscription 50%. On substitution of equation (21),

the relative deflection changes from equations (20) and (13) become

$$RDC(x_i, x_L) = \begin{cases} \beta\left[\zeta_{M_1}^{50\%}(x_L) + \left(\dfrac{g(x_1, x_L)}{u_0(x_1, x_L)}\right)\right] \text{ (damaged span)}, \\[4mm] \beta\, \zeta_{M_2}^{50\%}(x_L) \text{ (undamaged span)}. \end{cases} \qquad (22)$$

Or in a shorter form:

$$\text{RDC}(x_i, x_L) = \beta\,\text{RDC}^{50\%}(x_i, x_L), \quad i = \overline{1, m}, \qquad (23)$$

where RDC$^{50\%}$ is a referenced relative deflection change defined as follows:

$$RDC^{50\%}(x_i, x_L) = \begin{cases} \zeta_{M_1}^{50\%}(x_L) + \left(\dfrac{g(x_1, x_L)}{u_0(x_1, x_L)}\right) \text{ (damaged span)}, \\[4mm] \zeta_{M_2}^{50\%}(x_L) \text{ (undamaged span)}. \end{cases} \qquad (24)$$

For statically determinate beams, the RDC$^{50\%}$ function can be conveniently obtained in closed-form solutions as demonstrated in [4, 24]. This enabled damage severity calculation directly from the measured RDC, which is only valid for a particular beam type such as simply supported beams or cantilever beams. However, such closed-form mathematical expressions do not exist in multiple span beams due to the indeterminacy of the bending moment and the $g(x_1, x_L)$ function. An alternative approach to address this unavailability is proposed as follows.

Since $\zeta_{M_i}^{50\%}$, $g(x_1, x_L)$, $u_0(x_1, x_L)$ are independent of the flexural stiffness EI, it is apparent from (24) that the RDC$^{50\%}$ is a geometrical function and independent from the beam cross section and material properties. Therefore, RDC$^{50\%}$ can be obtained from any virtual FE beam model, whose span configuration is as same as the real beam, with arbitrary flexural stiffness EI. For bridge girders with constant EI, all the information required for the virtual model is the span lengths and support conditions of the real beam. The virtual beam model is named herein as the SSVB model. In practice, the SSVB can be a geometrically updated FE model of the real structure, which can be conveniently obtained from inspection and as-built documents.

A procedure to obtain the RDC$^{50\%}$ from the SSVB model is summarised as follows:

1. Develop an SSVB FE model whose configuration is as same as the real girder, with arbitrarily constant beam section and material properties.

2. Obtain the intact deflection vectors $u_{SSVB}^h(x, x_L)$ from the SSVB model under the same UPL applied to the real beam.

3. Once the damaged element is identified on the real beam using the damage locating criteria outlined in

Section 2.1.5, its location and length (a and b) are updated to the SSVB model with a virtual damage severity assigned as $\alpha = 50\%$.

4. Extract the deflection vectors $u_{SSVB}^{50\%}(x, x_L)$ from the virtual damaged SSVB model under the same UPL previously applied to obtain the undamaged $u_{SSVB}^h(x, x_L)$.

5. Calculate the referenced relative deflection change RDC$^{50\%}$ vectors following

$$\text{RDC}^{50\%}(x, x_L) = \left(\frac{u_{SSVB}^{50\%}(x, x_L) - u_{SSVB}^h(x, x_L)}{u_{SSVB}^h(x, x_L)}\right). \qquad (25)$$

After the referenced RDC$^{50\%}$ function is determined from equation (25), the damage severity of the real structure is estimated following the damage–severity–consistency (DSC) concept proposed by the present authors in [4, 5, 24], which can be summarised as follows. First, a DSC function is calculated by equation (26). Then, the damage severity derivative is calculated from equation (27) by averaging the DSC function. Subsequently, the damage severity coefficient is calculated for a specific UPL following equation (28). The final damage severity can be fine-tuned by averaging results obtained from some UPLs of interest.

$$\text{DSC}(x, x_L) = \left(\frac{\text{RDC}(x, x_L)}{\text{RDC}^{50\%}(x, x_L)}\right), \qquad (26)$$

$$\beta(x_L) = \overline{DSC}(x, x_L), \qquad (27)$$

$$\alpha(x_L) = \frac{(\beta(x_L))}{(1 + \beta(x_L))}. \qquad (28)$$

It should be noted that the accuracy of the damage quantification results relies on correctly identifying the damaged length (b) assigned to the SSVB model. This value is influenced by factors such as the availability of deflection measurements around the damage, the type of damage and measurement noise, which will be thoroughly explored in Sections 3–5. When distinct peaks appear at beam elements on the DC or RDC plots, a direct estimation of b is possible (see in Section 3), typically requiring sufficient beam deflection measurements around the damage locations. In other cases, estimating the damage length may require engineering judgement based on the nature of the damage and observed deflection change patterns. Examples (in Section 4) include assuming an effective length for a single open crack or adjusting the assumed damage location and length to discard false detections caused by measurement noise. Once the damage location and length are verified through a comprehensive visual inspection, the proposed SSVB method can accurately quantify damage (see in Section 5).

2.3. Locating and Quantifying Multiple Damage in Multispan Beams.

From the principle of superposition method, the DC and RDC caused by multiple damage locations are cumulative combinations of DC and RDC caused by each of the damage separately. Therefore, the damage locations can be identified at the peaks of the measured DC and RDC plots according to the proposed damage locating criteria in Section 2.1.5. Once the damaged elements are located, their damage severities are calculated using the SSVB concept for multiple damage as follows. From equation (23), the mathematical form of the RDC under multiple damage locations can be presented by

$$\text{RDC}(x_i, x_L) = \sum_{j=1}^{d} \beta_j(x_L)\text{RDC}_j^{50\%}(x_i, x_L), \qquad (29)$$

where d is the number of identified damaged elements. Equation (29) can be rewritten in matrix form as

$$\left[\text{RDC}^{50\%}(x_L)\right]_{N \times d} \{\beta(x_L)\}_{d \times 1} = \{\text{RDC}(x_L)\}_{N \times 1}, \qquad (30)$$

where N is the number of measurement points and $[\text{RDC}^{50\%}]$ is the matrix containing d referenced relative deflection change $\left\{\text{RDC}_j^{50\%}\right\}_{N \times 1}$ vectors obtained from the SSVB model under virtual damages. The damage severity derivatives β_j can be obtained by solving the system of N linear equations (30). Since the number of measurement points N is often higher than the number of damage locations d, the system of equations (30) is often overdetermined (the equations outnumber the unknowns). For an overdetermined system, an approximate solution using the method of ordinary least squares (the least square solution) can be given as follows [37]:

$$\{\beta(x_L)\}_{d \times 1} = \left(A^T A\right)^{-1} A^T b, \qquad (31)$$

where A denotes the coefficient matrix $[\text{RDC}^{50\%}(x_L)]$ and **b** denotes the vector of constants $\{\text{RDC}(x_L)\}$.

Finally, the damage severity coefficients α_j are calculated using equation (28) for each of the damaged elements.

2.4. Use of Output-Only MF-Based Proportional Deflection Changes (PDCs).

Above methodology can be perfectly applicable for static deflections under traditional static force-controlled testing conditions. However, as stated earlier, it is not always possible to carry out such static tests, especially on highway bridges with high traffic volumes. Le et al. [24] demonstrated that the use of indirect deflections obtained from MF matrices can substitute the static deflections for DI purposes. In this research, we focus on another practical case when the true MF matrices are not available under output-only vibration tests. The proportional deflection concept is thereby incorporated with above-proposed methodology to extend its applicability to important cases when only ambient (operational) vibration test results conducted in highway bridges are available.

Let us start with the following relationship between static deflection and the structural flexibility [36]:

$$u = \text{F}\, f, \qquad (32)$$

where f is an arbitrary static load applied to the structure and F is the structural flexibility matrix, which can be approximated to the MF matrix with sufficient accuracy by using a few modes of vibration as follows [38, 39]:

$$\text{F} \approx \text{MF} = \sum_{i=1}^{n} \frac{1}{\omega_i^2} \frac{1}{m_i} \psi_i \psi_i^{\text{T}}, \qquad (33)$$

where MF is the $N \times N$ MF matrix, N is the number of DOF of the structure, ω_i, ψ_i and m_i are the ith modal frequency, mode shape and modal mass obtained from output-only vibration tests and n is the number of measured mode ($n \leq N$). The "$\approx$" relationship becomes "$=$" when all modes of vibration are used, which is impractical. However, for damage detection purposes, it has been widely accepted that a few early modes are sufficient. ψ_i are often chosen to be unit mode shapes having unit length ($\psi_i^{\text{T}}\psi = 1$). In addition, for Euler–Bernoulli beams with constant or nearly constant cross section, the mass matrix M can be reasonably assumed to be diagonal [40], and the lumped mass m is distributed equally among the DOFs of the system. Therefore, the ith modal mass is formulated and transformed to

$$m_i = \psi_i^{\text{T}} M \psi_i = \psi_i^{\text{T}} \text{Diag}(m) \psi_i = m(\psi_i^{\text{T}} \psi_i) = m. \qquad (34)$$

On substitution of m_i to equation (33), the MF matrix becomes

$$\text{MF} = \frac{1}{m} \left(\sum_{i=1}^{n} \frac{1}{\omega_i^2} \psi_i \psi_i^{\text{T}} \right). \qquad (35)$$

While the above equation is only valid for Euler–Bernoulli beams with uniform mass distribution, this characteristic is notably relevant to highway bridge girders. The unavailability of the modal mass in output-only modal tests naturally leads to the construction of the MF-like term

within the parenthesis () in equation (35), which is proportional to MF and named as the PMF matrix as follows:

$$\text{PMF} = \sum_{i=1}^{n} \frac{1}{\omega_i^2} \psi_i \psi_i^{T} = m \, \text{MF} \approx m \, \text{F}. \tag{36}$$

By deducing equation (32), a MF-based proportional deflection u_P can be extracted from the PMF, which differs from the exact static deflection by the scalar m:

$$u_P = \text{PMF} \, \mathbf{f} \approx m \, (F \, f) = m.u. \tag{37}$$

Assume structural damage does not cause significant changes in mass. By comparing the undamaged ("h") and damaged ("d") states, the relationship between MF-based PDC and the true static deflection change DC is given by

$$\text{PDC} = u_P^d - u_P^h = \left(\text{PMF}^d - \text{PMF}^h\right) \mathbf{f} = PMFC \, \mathbf{f} \approx m\left(u^d - u^h\right) = m \, DC, \tag{38}$$

where PMFC is the proportional modal flexibility change matrix. Similarly, the relationship between MF-based proportional relative deflection change (PRDC) and the static RDC is derived as

$$\text{PRDC} = \frac{u_P^d - u_P^h}{u_P^h} = \left(\text{PMFC} ./ \text{MF}^h\right) \mathbf{f} = \text{PRFC} \, \mathbf{f} \approx \left(\frac{m\left(u^d - u^h\right)}{m \, u^h}\right) = \text{RDC}, \tag{39}$$

where PRFC is the proportional relative modal flexibility change and proportional relative flexibility change, and the notation "./" denotes the elementalwise division. It is evidenced from equations (38) and (39) that the MF-based PDC is proportional to the static DC and the MF-based PRDC is approximately equal to the static RDC. These mean all the observable damage locating criteria developed for static DC and RDC in Section 2.1.5 are maintained when the output only MF-based PDC and RDC are used. In addition, the MF-based PRDC can substitute the static RDC to quantify the damage following the method proposed in Section 2.2. For convenience, the term MF-based RDC is used hereafter to replace MF-based PRDC.

Figure 3 illustrates a convenient way to extract the MF-based proportional deflection from the proportional flexibility matrices when virtual UPLs are used as the static load f. Accordingly, the MF-based $u_P(x, x_L = x_i)$ vector under the UPL acting at the ith DOF is simply the ith column of the PMF matrix. The operation is carried out for both undamaged and damaged states. Consequently, a series of MF-based PDC and RDC vectors under multiple UPLs can be extracted without the need to conduct multiple static deflection tests.

It should be noted that the poor signal-to-noise ratio of flexural deflections and mode shapes near supports may affect the sensitivity of the method in identifying damage at these locations. Addressing this will be part of the authors' future studies. Readers interested in this topic can find relevant literature, such as [22], which introduces approaches such as the damage-induced chordwise deflection for detecting and locating damage in these regions.

3. Numerical Verification on a Two-Span Beam

This section illustrates the performance of the proposed method through numerical verifications on a two-span reinforced concrete continuous beam model (Figure 4). The model is divided into 24 beam elements and 25 nodes. Young's modulus, Poisson's ratio and mass density of the material are 35 GPa, 0.2 and 2500 kg/m³, respectively. The beam cross section is a rectangle of 0.3×0.6 m. Two damage scenarios were simulated by reducing the beam member stiffness or flexural rigidity EI at different beam elements, including single and double-damage cases (Table 1). The stiffness reduction was numerically simulated using a popular method in damage detection research by assigning a reduction on the material Young's modulus while keeping the beam section unchanged. An SSVB model of the beam was also developed for damage quantification, with geometrical and material properties summarised in Table 2. The SSVB model configuration is as same as the real beam, yet its section and material properties are intentionally set differently to illustrate the arbitrariness of the flexural rigidity according to the proposed method.

Figure 5 illustrates the resultant mode shapes of the beam in the intact state. Mode shapes in the damaged states are visually similar to the undamaged ones and are therefore omitted for brevity. Table 3 compares the first four natural frequencies of the real beam in the undamaged state and the two damage scenarios. The reduction in the natural frequencies reflects the existence of damage. The resultant modal frequencies and unit mode shapes from both the real beam and SSVB models were then used to calculate the proportional flexibility matrices and extract the proportional deflections following a procedure illustrated in Figure 3.
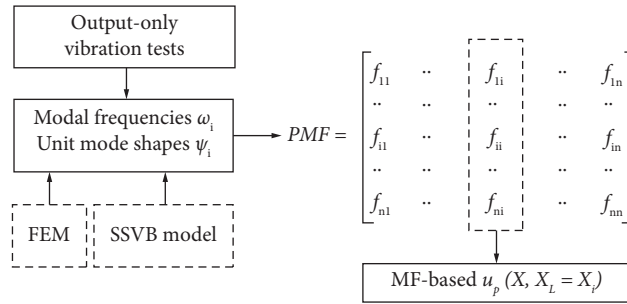
Figure 3: Extraction of MF-based deflections from PMF matrices.
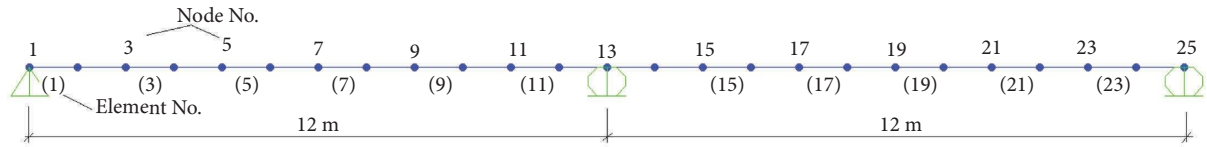

Figure 4: The two-span continuous beam model.

Table 1: Damage scenario definition.

Damage case	D1.1		D1.2
Created damaged element(s)	(19)	(7)	(19)
Created damage severity*	15%	15%	30%

*Flexural stiffness reduction.

Table 2: Comparison of real beam and the SSVB.

Properties	Real beam	SSVB model
Beam span lengths	2×12 m	2×12 m
Material	Concrete	Concrete
Young's modulus	35 GPa	30 GPa
Cross section	30×60 cm	30×80 cm
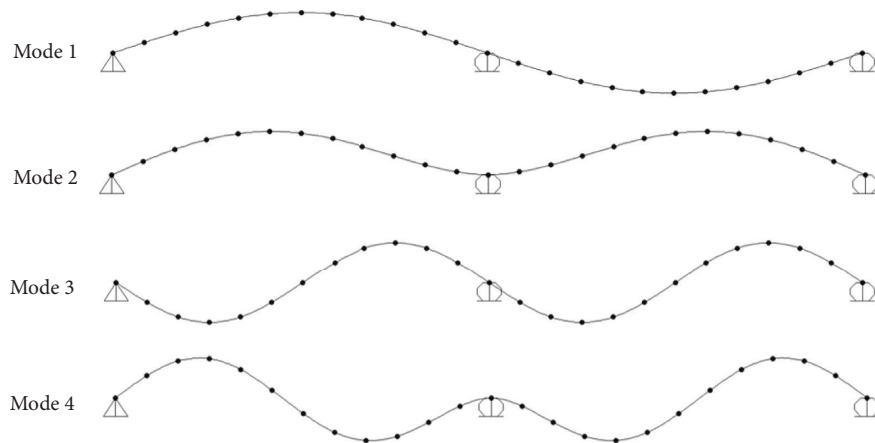
Figure 5: The first four bending mode shapes in undamaged state.

Figure 6 demonstrates the DI results for the single damage D1.1 using changes in MF-based PDC and RDC. Three observable damage locating criteria are clearly shown in Figures 6(a) and 6(b). First, it can be observed from Figure 6(a) that all the MF-based PDC plots under various UPLs present a consistent pattern with a smooth curve on the first span and a peak on the second span of the beam. This indicates the existence of a single damage on the second

TABLE 3: Natural frequencies of the beam model (Hz).

Mode No.	Intact	D1.1	D1.2
1	7.05	7.00	6.88
2	10.95	10.89	10.77
3	27.94	27.92	27.87
4	35.03	35.014	34.90

span at beam element No. 19 according to the first damage locating criterion proposed in Section 2.1.5. In addition, the RDC plots in Figure 6(b) also reveal an abrupt change (peak) at beam element No. 19 on the second span and depict nearly constant values on the first span of the beam. This pattern confirms the occurrence of damage at element 19 relevant to the second damage locating criterion. Further, the magnitudes of the PDC and RDC plots are largest when the UPL is applied at nodes 19 and 20, which is pertinent to the third damage locating criterion. Therefore, the damage detection results accurately reflect the developed damage locating concepts for continuous beams as presented in Section 2.1.5.

Given that deflections are extracted at all degrees of freedom, both PDC and RDC plots clearly depict damaged elements. This enables the precise determination of the damage length, a crucial factor in estimating damage severity using the SSVB method. To quantify the damage, a damaged element is created at the beam element No. 19 on the SSVB model (same position as the identified damage above), with a virtual damage severity of 50%. The referenced $\text{RDC}^{50\%}$ vectors at selected UPLs are then numerically obtained from equation (25) following the procedure provided in Section 2.2 using the MF-based proportional deflections extracted from the SSVB model. As an illustration, Figure 6(c) shows the MF-based RDC (from real beam) and $\text{RDC}^{50\%}$ (from SSVB) together with the consistency DSC function which is the ratio between RDC and $\text{RDC}^{50\%}$ following equation (26). It shows that DSC is nearly constant among all the node numbers, which means that the measured RDC is proportional to the $\text{RDC}^{50\%}$, and that being perfectly relevant to equation (23). As defined in equation (27), the damage severity derivative $\beta = 0.18$ is obtained by averaging the DSC values among the nodes. Finally, from equation (28), the damage severity coefficient is conveniently estimated to be 15.3% as shown in Figure 6(d), which is very close to the correct value of 15%. Damage quantification results under other UPLs were also found to be close to 15%. Therefore, the proposed method accurately locates and quantifies the single damage case D1.1.

Figures 7(a), 7(b) and 7(c) illustrate the procedure to identify the double damage case D1.2, with two damaged elements occurring on different spans, whereas Figure 7(d) shows the corresponding damage quantification result. The MF-based PDC plots under various UPLs (Figure 7(a)) clearly indicate two peaks at beam elements No. 7 and 19. The figure also indicates that the peak's magnitudes of the PDCs on the first span are larger when the UPL is closer to Node 8 (beam location 7 m). Similarly, the PDC peak's magnitude on the second span is the largest when the UPL is

at Node 19 (beam location 18 m). Therefore, the existence of damage at beam elements No. 7 and No. 19 is determined according to the first and third damage locating criteria proposed in Section 2.1.5. Furthermore, the existence and locations of the two damaged elements are confirmed by observing the MF-based RDC plots under UPLs at Node No. 8 and No. 19 presented in Figure 7(b). In this scenario, there are no constant parts on the RDC plots since both spans are subjected to damage. To quantify this double damage case, it is necessary to calculate two referenced relative deflection change vectors $\text{RDC}_i^{50\%}$ corresponding to each of the damage elements (Figure 7(c)). To obtain the $\text{RDC}_1^{50\%}$ vector for the first damage, the bending stiffness EI of the beam element No. 7 on the SSVB model is reduced by 50%. The MF-based deflection vectors before and after the damage u_{SSVB}^h and $u_{SSVB}^{50\%}$ are then used to calculate the $\text{RDC}_1^{50\%}$ following equation (25). Analogously, the referenced $\text{RDC}_2^{50\%}$ vector for the second damage is obtained from simulating the second damage at beam element No. 19. The resultant $\text{RDC}_1^{50\%}$, $\text{RDC}_2^{50\%}$ and RDC vectors presented in Table 4 are substituted into equation (30), resulting in a system of 22 linear equations as follows (22 is the number of beam nodes excluding the three supports):

$$\left[\text{RDC}^{50\%}\right]_{22x2} \{\beta\}_{2x1} = \{\text{RDC}\}_{22x1}. \tag{40}$$

The system is overdetermined since it has 22 equations and only 2 unknowns. As explained in Section 2.3, the damage severities can be estimated by the method of least squares as follows:

$$\{\beta\}_{2x1} = \left\{ 0.1838 \quad 0.4432 \right\}^T. \tag{41}$$

The second norm of the marching vector $\|[\text{RDC}^{50\%}]\{\beta\} - \{\text{RDC}\}\| = 7.9106E - 04 \sim 0$, which indicates that the above approximate solution is accurate. Finally, from equation (28), the damage severities are derived as $\alpha_1 = 15.53\%$ and $\alpha_2 = 30.71\%$ using the data under an UPL acting at node No. 8. Similar damage quantification results under other UPLs are summarised in Table 5 showing consistent results with minimal standard deviations. The average damage severity values among all UPLs are $\alpha_1 = 15.7\%$ and $\alpha_2 = 30.6\%$ with minor errors compared to correct values of 15% and 30% for damage 1 and damage 2, respectively.

From the above numerical verifications, the developed DBDI method incorporating SSVB model demonstrated highly accurate damage detection, localisation and quantification capabilities in both single and multiple damage scenarios in multiple span beam models.
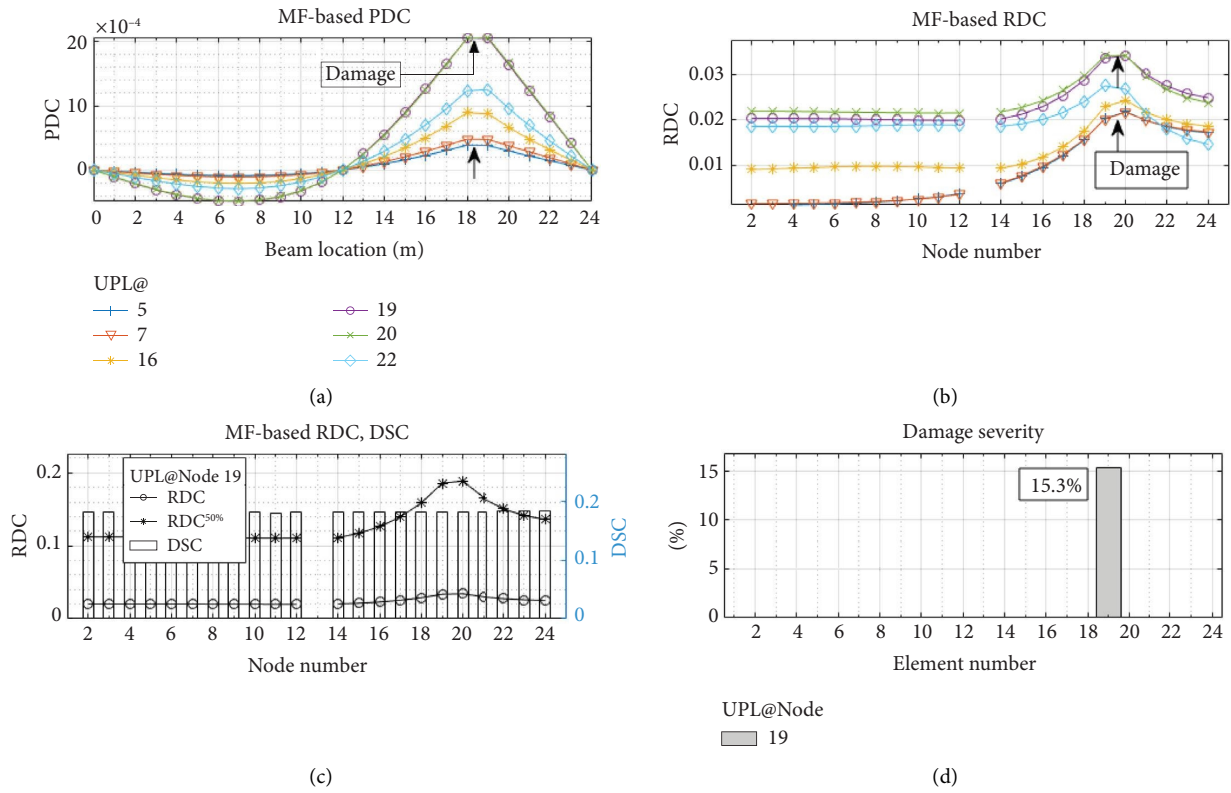
(a)

(b)

(c)

(d)

FIGURE 6: Damage detection results in D1.1 scenario: (a) PDC under different UPLs; (b) corresponding RDC plots; (c) RDC and DSC plots under UPL at node No. 19; (d) damage quantification result.
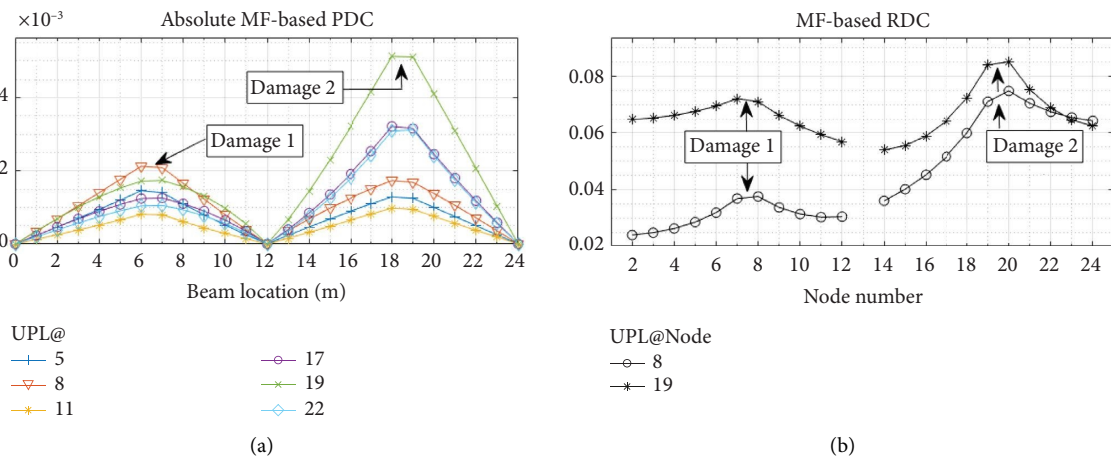

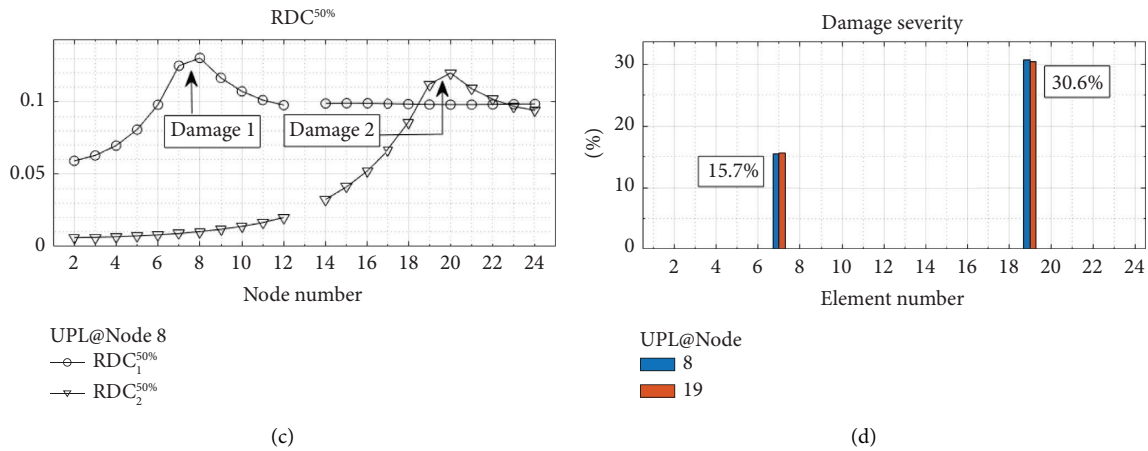
(a)

(b)

FIGURE 7: Continued.

(c)

(d)

FIGURE 7: Damage detection results for D1.2 scenario: (a) PDC under different UPLs; (b) RDC plots under UPLs at nodes No. 8 and 19; (c) $RDC^{50\%}$ plots under UPL at node No. 8; (d) damage quantification result.

TABLE 4: $RDC^{50\%}$ and RDC values under the UPL at Node 8*.

Node No.	$RDC_1^{50\%}$	$RDC_2^{50\%}$	RDC	Node No.	$RDC_1^{50\%}$	$RDC_2^{50\%}$	RDC
2	0.1055	0.0101	0.0240	14	0.1167	0.0334	0.0360
3	0.1100	0.0101	0.0248	15	0.1169	0.0426	0.0401
4	0.1180	0.0101	0.0263	16	0.1174	0.0539	0.0452
5	0.1302	0.0102	0.0285	17	0.1180	0.0681	0.0517
6	0.1482	0.0104	0.0319	18	0.1186	0.0866	0.0600
7	0.1748	0.0108	0.0368	19	0.1190	0.1114	0.0710
8	0.1771	0.0115	0.0376	20	0.1190	0.1193	0.0748
9	0.1532	0.0125	0.0337	21	0.1188	0.1095	0.0705
10	0.1365	0.0140	0.0314	22	0.1183	0.1027	0.0674
11	0.1250	0.0162	0.0303	23	0.1178	0.0983	0.0654
12	0.1178	0.0195	0.0305	24	0.1175	0.0957	0.0643

*RDC values at beam supports (node No. 1, 13 and 25) do not exist.

TABLE 5: Damage severity estimation from different UPLs.

Damaged elements	Severity	UPL at node No.						Average	Standard deviation
		5	8	11	17	19	22		
Damage 1	β_1	0.1828	0.1838	0.1844	0.1846	0.1861	0.1899	0.185	0.002
	α_1	15.46%	15.53%	15.57%	15.59%	15.69%	15.96%	15.7%	0.16%
Damage 2	β_2	0.4439	0.4432	0.4382	0.4391	0.4390	0.4373	0.440	0.003
	α_2	30.74%	30.71%	30.47%	30.51%	30.51%	30.43%	30.6%	0.12%

4. Numerical and Experimental Verifications on a Real Slab-on-Girder Bridge

In this section, the proposed DBDI method is numerically and experimentally verified on a complex girder bridge structure. The structure of interest is the I-40 slab-on-girder bridge, which has been a well-known benchmark for SHM studies and DI verifications originally reported by Farrar et al. [41]. Section 4.1 describes the configuration of the bridge and the benchmark modal testing results serving as input data for this research. A FE model of the bridge is developed in Section 4.2 for developing its SSVB model in Section 4.3 and numerical verifications in Section 4.4. Finally, the benchmark experimental modal data will be used

to assess the real damage on the bridge in Section 4.5 and results will be compared to numerical assessment in Section 4.2.

4.1. The Benchmark I-40 Bridge and the Experimental Modal Data.

Figures 8, 9 and 10 illustrate the configuration of the I-40 slab-on-girder bridge constructed in the early 1960s over the Rio Grande River in New Mexico, USA. The tested part of the bridge consists of three continuous spans with a total length of 129 m. As schematised in Figures 9 and 10, the superstructure of the bridge consists of a 13.05 m-wide reinforced concrete slab, two 3.11 m-deep steel plate girders and a system of stringers and floor beams. The dimensions of

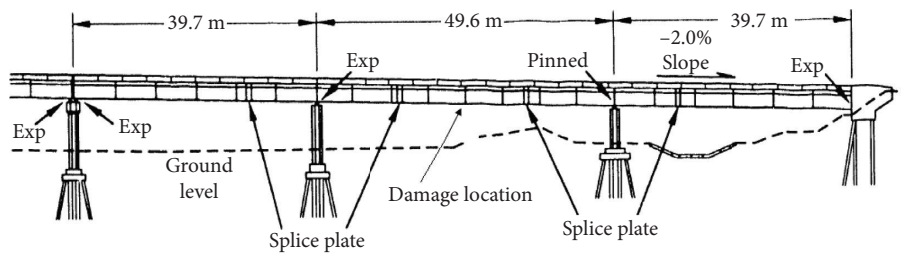FIGURE 8: I-40 bridge in Albuquerque, USA [41].

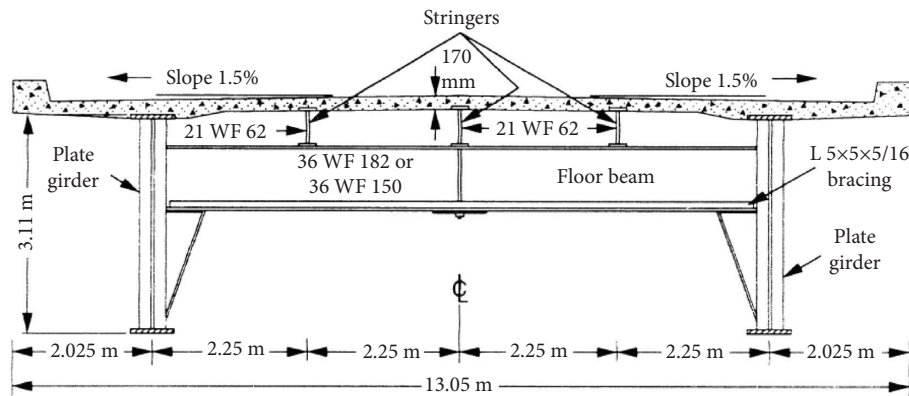FIGURE 9: Elevation view of the I-40 bridge [41].

FIGURE 10: Main structural components [41] (draw not to scale).

the plate girder section are given in Figure 11(a). The stringers are supported by a system of 36-floor beams framing into the girders. The girders are supported by roller and pinned supports placed on the substructure. Interested readers can refer to [41, 42] for a more detailed description of the bridge.

As described in Farrar et al. [41], four levels of damage were introduced near the midpoint of the middle span of the north plate girder (Figure 12) by cutting its web and lower flange. Schematic of the three last damage cases, E-2 to E-4, is depicted in Figures 11(b), 11(c), 11(d) and 13. A series of forced and ambient vibration tests on the bridge were conducted by the Los Alamos National Lab in 1993 in the undamaged and damage states for modal parameter identification [41]. The acceleration responses of the bridge were measured at 26 locations distributed along the two plate girders as shown in Figure 12. The first three damage scenarios were reported to have small effects on the structural responses and the resultant minor changes in modal frequencies were reportedly masked by environmental effects [43, 44]. To the best of the authors' knowledge, previous literature has not successfully achieved a comprehensive quantification of these damage cases. Therefore, the most severe damage case (E-4) will undergo both numerical and experimental evaluation, while less severe cases (E-2 and E-3) will be assessed numerically in this study. This approach facilitates the quantification of the actual damage in E-2 and E-3, supporting the hypothesis that their minor severity makes them challenging to detect in real-world testing.

Table 6 summarises the measured natural frequencies of the first six modes in the intact and the fourth damage case E-4. As can be seen from the table, there was a significant
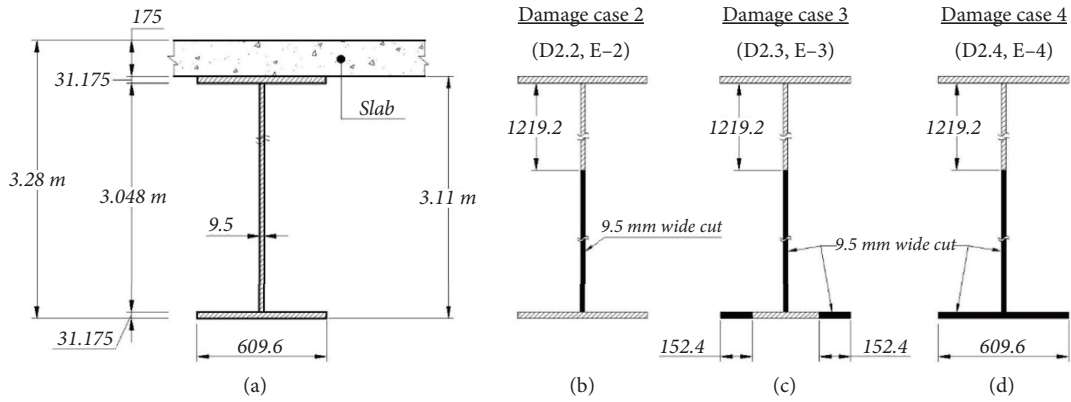
FIGURE 11: Cross section of the plate girder: (a) slab-on-girder section; (b–d) schematic of damage scenarios inflicted in steel girder (adapted from [41, 43], dimensions in mm).
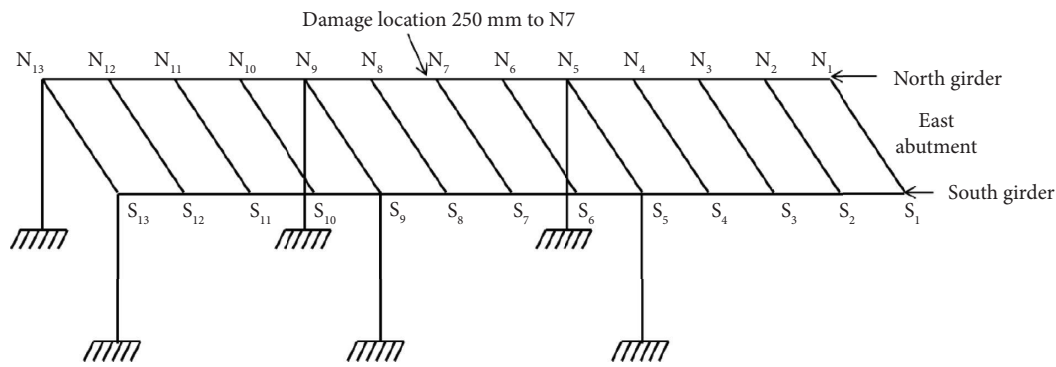
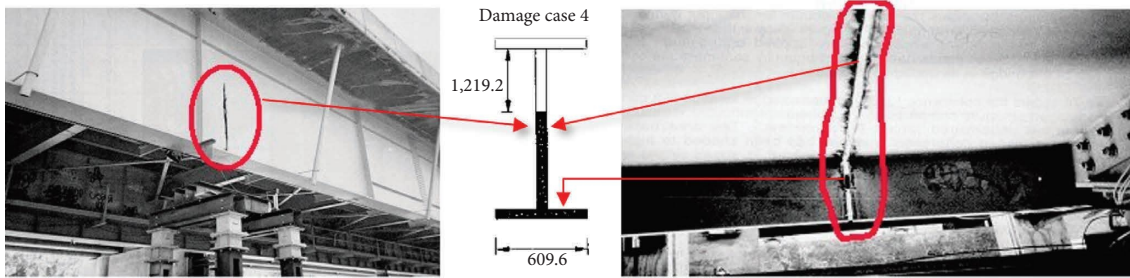FIGURE 12: Sensor layout and location of damage (after [41]).

FIGURE 13: The fourth damage (after [41, 43]).

TABLE 6: Experimental natural frequencies (Hz) (adopted from [41]).

Test damage scenarios	Modes					
	1	2	3	4	5	6
Undamaged	2.48	2.96	3.50	4.08	4.17	4.63
Damage case E-4*	2.27 (−8.5%)	2.83 (−4.4%)	3.49 (−0.3%)	3.99 (−2.2%)	4.15 (−0.5%)	4.52 (−2.4%)

*Values in (...) indicate relative changes (%) compared to undamaged state.

drop in the fundamental frequency equivalent to a −8.5% relative change, which normally indicates that severe damage had occurred on the structure. The measured unit mode shapes of the bridge in the undamaged state are presented in Figure 14 and compared with the numerical mode shapes obtained later from the FE analysis in Section 4.2.

4.2. Development of the I-40 Bridge FE Model. A FE model of the I-40 bridge was developed using the SAP2000 software based on geometrical information and modal testing results described in Section 4.1. Numerical investigation from this model will test the performance of the proposed VBDI method on a complex structure and estimate the damage severity of the simulated damage scenarios for later

(a)   (b)
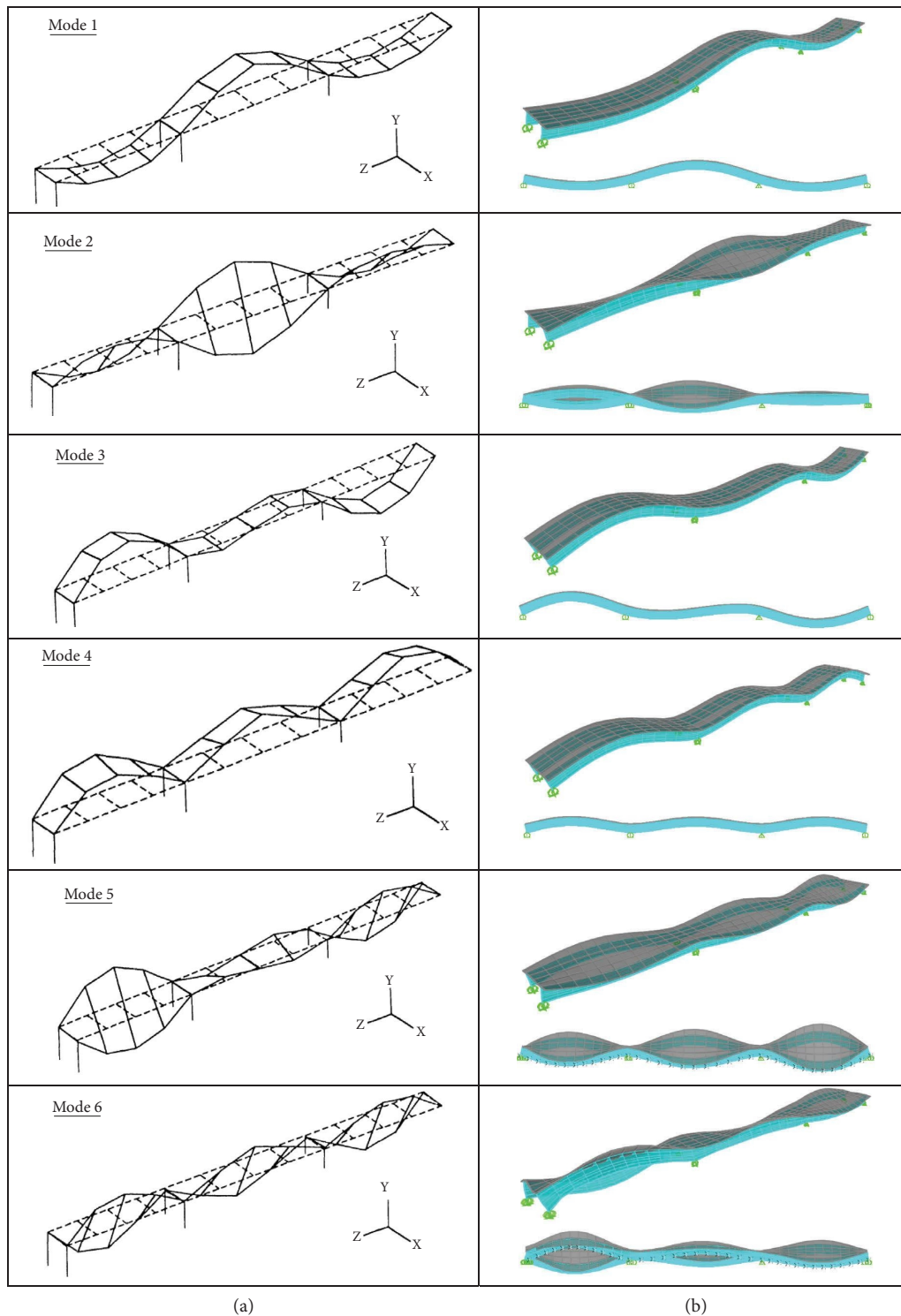
FIGURE 14: Experimental (a) verses FE analysis ((b), see Section 4.2) undamaged mode shapes of I40 bridge.

experimental verification. Since this study focuses on DI on the bridge girders, it is reasonable to exclude the substructure in the FE model (Figure 15).

Each span of the bridge was subdivided into 12 equal segments resulting in 36 slab-girder composite portions (Figure 16). Modal parameters are extracted from 37 output points at the bottom flange of the girders, some of which are at the same positions as the sensors as described in the field test (Figure 12). Material properties are presented in Table 7, which were manually adjusted to minimise the differences between the modal parameters of the FE analysis and experimental results. Figure 14 compares numerical mode shapes with testing results in the undamaged state, which shows satisfactory agreement in terms of mode shape
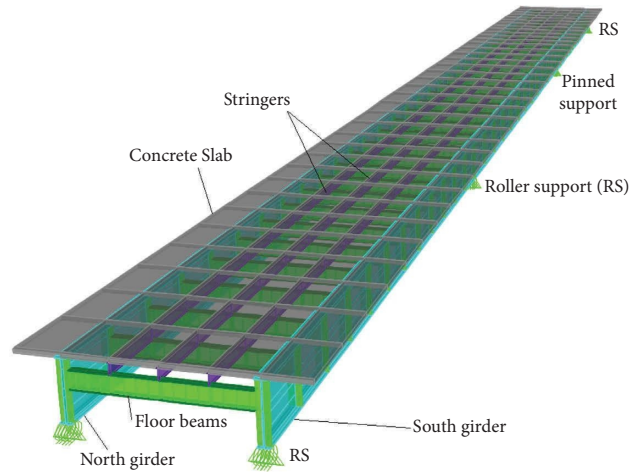
FIGURE 15: 3D view of the I-40 slab-on-girder bridge FE model.
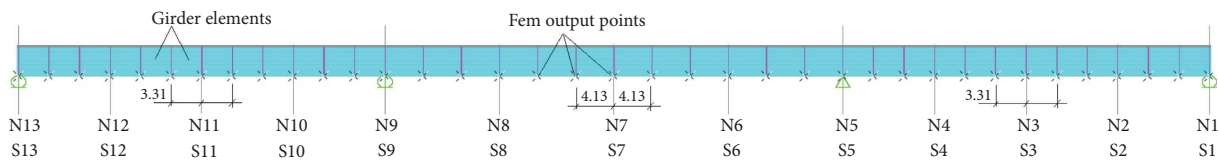
FIGURE 16: FE output points compared to experimental sensor locations (N1 to N13: sensors on North girder, S1 to S13: sensors on South girder, to see with Figure 12).

TABLE 7: Material properties of the validated FE model.

Structural components	Young's modulus (GPa)	Poisson's ratio	Mass density (kg/m^3)
Concrete slab	24	0.2	2500
Steel girders, strings, floor beams	200	0.3	7850

patterns. Table 8 (column 2) shows the numerical natural frequencies, with acceptable relative differences compared to the testing results of only 1.6%, 2.2% and 4.3% for the first three flexural modes (modes 1, 3 and 4). The first and the third torsional modes (modes 2 and 6) also have an acceptable error of ~6%. The largest relative difference comes from the second torsional mode (mode 5) of 14.6%, which can be explained by the fact that obtaining high accurate experimental results for higher-order modes in complex structures is challenging. Since flexural modes are the main contributors to the deflection behaviours of bridge girders, the developed FE model can be considered a good representation of the real bridge for numerical damage investigation purposes.

Four damage scenarios were then numerically simulated on the validated I-40 FE model as described in Table 9. The first damage scenario (D2.1) was generated by reducing the member stiffness of both concrete slab and steel girder by 30% (damage severity $\alpha = 30\%$) over an 8.26-m-length of the slab-girder portions at the middle region of the middle span (Figure 17). The analysed natural frequencies of D2.1 are presented in Table 8 (column 3) showing slightly decreases compared to the FE undamaged results. The known extent of damage, in this case, provides a perfect scenario to validate the accuracy of the proposed method for quantifying damage in complex structures.

The last three damage scenarios (Figure 18), denoted as D2.2, D2.3 and D2.4, were numerically created by removing material from the girder's web and flange in a manner similar to the actual cuts of the three field test damage cases E-2, E-3 and E-4 shown in Figures 11 and 13. The resultant numerical natural frequencies are presented in Table 8. The minor relative decreases in the first natural frequencies of −0.2% (D2.2) and −0.3% (D2.3) indicate small stiffness reduction in the second and third cases. By contrast, there is a significant relative decrease of −8.8% in the fundamental natural frequency of the last damage case D2.4 (Table 8, column 6), which closely approximates the field test result of −8.5% (Table 6). Since the known 30% damage severity in D2.1 only causes a −1.3% relative reduction in the first natural frequency, a relative decrease of −8.8% in D2.4 preliminarily indicates that this should be a much more severe damage scenario. The unknown severity of damage in D2.2, D2.3 and D2.4 scenarios necessitates the quantification to give a reference for later experimental study, and the proposed DBDI method will be employed for this task in the following sections. The model of opened cracks studied by Christides and Barr [45] is applied to estimate the stiffness reduction in the crack vicinity. As suggested by Sinha et al. [46], the total effective damage length can be taken as three times the

TABLE 8: Numerical natural frequency (Hz).

Mode number	FE damage scenarios					Note
	Intact[1]	D2.1[2]	D2.2[2]	D2.3[2]	D2.4[2]	
(1)	(2)	(3)	(4)	(5)	(6)	(7)
1	2.441 (−1.6%)	2.409 (−1.3%)	2.436 (−0.2%)	2.433 (−0.3%)	2.227 (−8.8%)	1st flexural mode
2	3.132 (5.8%)	3.118 (−0.5%)	3.150	3.149	3.056 (−2.4%)	1st torsional mode
3	3.572 (2.1%)	3.568 (−0.1%)	3.571	3.571	3.568 (−0.1%)	2nd flexural mode
4	4.256 (4.3%)	4.240 (−0.4%)	4.254	4.252	4.160 (−2.3%)	3rd flexural mode
5	4.777 (14.6%)	4.761 (−0.3%)	4.774	4.772	4.686 (−1.9%)	2nd torsional mode
6	4.919 (6.2%)	4.909 (−0.2%)	4.919	4.919	4.914 (−0.1%)	3rd torsional mode

[1]Values in (...) are relative changes compared to undamaged test results in Table 6.
[2]Values in (...) are relative changes compared to numerical intact results in column 2.

TABLE 9: Damage scenario definition for the I-40 bridge investigations.

Damage case	D2.1	D2.2	D2.3	D2.4
Damage type	Reducing member flexural stiffness	Cutting/removing material on girder's web and flange (Figures 13 and 18)		
Damage severity	30%	To be determined		
Damaged length	8.26 m (Figure 17)	To be estimated as 9.84 m (three times the girder's height)		
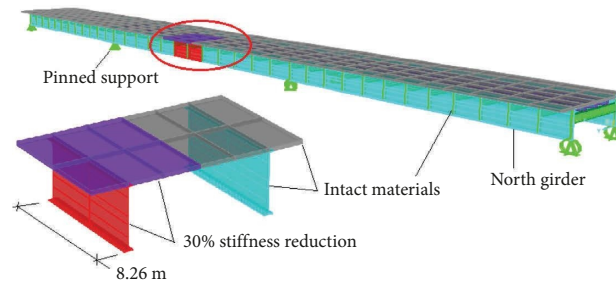
FIGURE 17: Simulation of damage scenario D2.1.
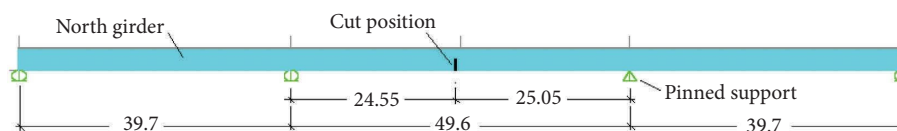
FIGURE 18: Damage cases D2.2, D2.3 and D2.4 (dimensions: m; revisit Figure 13 for detailed damage description).

girder height. With the girder's height of $H = 3.28$ m (Figure 11), the effective damage length for these cases will be taken as 9.84 m (Table 9).

4.3. The SSVB Model of the I-40 Bridge Girders. A FE SSVB model was developed to compute the reference RDC^50% for damage quantification in the numerical and experimental studies on the I-40 bridge. The beam has the same span and support configuration as the I-40 bridge's main girder as shown in Figure 19. The beam material was selected as concrete, with a rectangle cross section of 1.0 m × 3.0 m for modelling simplicity. Young's modulus, Poisson's ratio and mass density of the concrete were 35 GPa, 0.2 and 2500 kg/m^3, respectively. Figure 20(a) illustrates the model with virtual damage severity of 50% applied to an 8.26 m long

portion to quantify the damage case D2.1. Similarly, Figure 20(b) presents a virtual model with 50% damage assigned over a 9.84 m long portion to quantify the severity of the cut-like damage cases D2.2, D2.3 and D2.4 as described in the previous section.

4.4. Numerical Verification of the I-40 FE Model. The mass-normalised mode shapes extracted from the FE model and SSVB model were converted into unit mode shapes to simulate output-only modal data extracted from ambient vibration tests. The first three bending and three torsional modes of the I-40 FE model were used to calculate the MF-based proportional deflections, while the first three bending modes of the SSVB model were used to calculate the referenced RDC^50% (since torsional modes do not exist in 2-dimensional SSVB model).
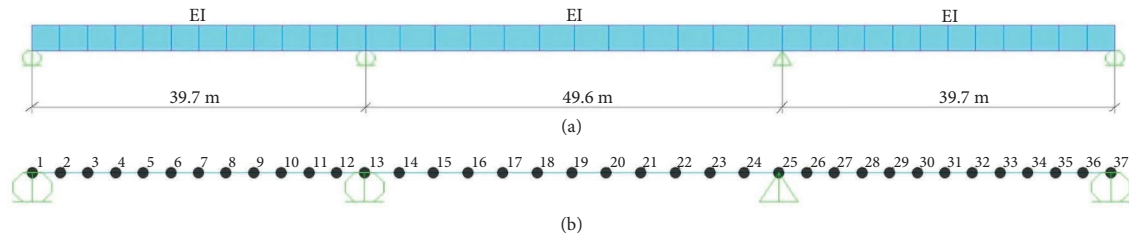
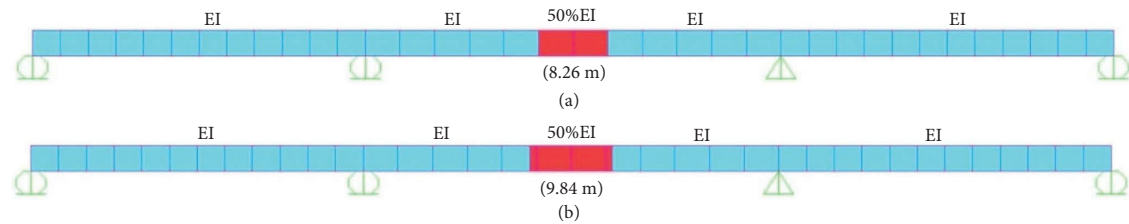FIGURE 19: The SSVB model in the undamaged state: (a) configuration; (b) node number.

FIGURE 20: Referenced damage states on the SSVB: (a) for D2.1; (b) for D2.2, D2.3, D2.4, E-4.

Figure 21 illustrates the DI results for the first damage case D2.1. For the North girder (Figure 21(a)), both MF-based PDC and RDC plots clearly reveal an abrupt peak at the simulated damaged portion. In addition, the magnitude of the PDC's peak is largest under UPLs applied around the damaged region. Therefore, the simulated damage was accurately detected and located according to the three proposed damage locating criteria. The damage severity consistency vector DSC under UPL at node 19 (Figure 21(a), second from top) was then calculated as the ratio between the RDC and $RDC^{50\%}$ following equation (27). Less obvious consistent values of the MF-based DSC on the undamaged spans compared to the damaged span reflect the structural complexity and limited number of modes used to calculate the MF-based PDC. Nevertheless, the average DSC value $\beta = 0.415$ provides satisfactory damage severity of $\alpha = 29.3\%$, with negligible error compared to the simulated value of 30%. For the South girder, DI results in Figure 21(b) show no abrupt peak on either the PDC or RDC plots, and therefore no damage was detected according to the developed theory, which is relevant to the fact that no damage was created on this girder. Therefore, the proposed method demonstrates excellent DI and quantification capabilities in the complex girder bridge model using the SSVB concept.

The method was then employed to assess the damage cases D2.2, D2.3 and D2.4, where damage severity was unknown in advance. Figure 22 shows the DI results for D2.3 and D2.3 scenarios for the North girder, while corresponding results for the South girder similar to Figure 21(b) are omitted for brevity. The figures show correct damaged locations are detected and very small damage severity predicted, being 4.8% and 6.2%, respectively, which correctly reflect the little changes in natural frequencies depicted in Table 8. In fact, such small damage severity can be easily masked by environmental changes and measurement errors. This explains the difficulty in identifying actual damage cases E-2 and E-3 using real-world experimental data of the I-40 bridge reported in the literature.

The method was then applied to assess the last damage case D2.4, where the damage level was expected to be large. Damage assessment results for the North girder are presented in Figure 23(a). Three damage locating criteria can be observed from the figure: (1) MF-based PDC plot shows a sharp peak at beam location 64.5 m in the middle of the second span, (2) MF-based RDC plot shows a sharp peak at node No. 19 on the middle span and nearly constant portions on the side spans and (3) magnitudes of the PDC and RDC are largest when the UPL is applied near node 19. Therefore, the single damage was correctly located at the cut position around node No. 19 of the middle spans. As stated earlier, an equivalent damage length of three times the beam height is selected to quantify the damage severity. The referenced MF-based $RDC^{50\%}$ was then calculated from the SSVB model described in Section 4.3. From the RDC and $RDC^{50\%}$, the damage extent was estimated to be 67.2%, which is indeed severe damage in reality. For the South girder, results of MF-based PDC and RDC in Figure 23(b) indicate no abrupt peak, and therefore the damage state was correctly discarded on this girder.

4.5. Experimental Verification on the I-40 Bridge. From six available experimental natural frequencies and unit mode shapes, the output-only MF-based PDC and relative deflection change RDC under various UPLs are plotted in Figures 24(a1) and 24(a2). By observing the MF-based PDC and RDC plots, there is a clear peak at beam location 65 m (node No. 19, element No. 18-19) near the mid-region of the second girder span under all the UPLs. There is also another clear peak at node No. 31 (element No. 30-31) on the MF-based RDC plots under the UPL at node No. 7 and 19. However, when visiting the RDC plot under the UPL at node No. 31, the peak at this point disappears. This is unexpected based on the third damage locating criterion (Section 2.1.5), which suggests a larger peak's magnitude should appear when the UPL is applied closer to the damage. Similarly,
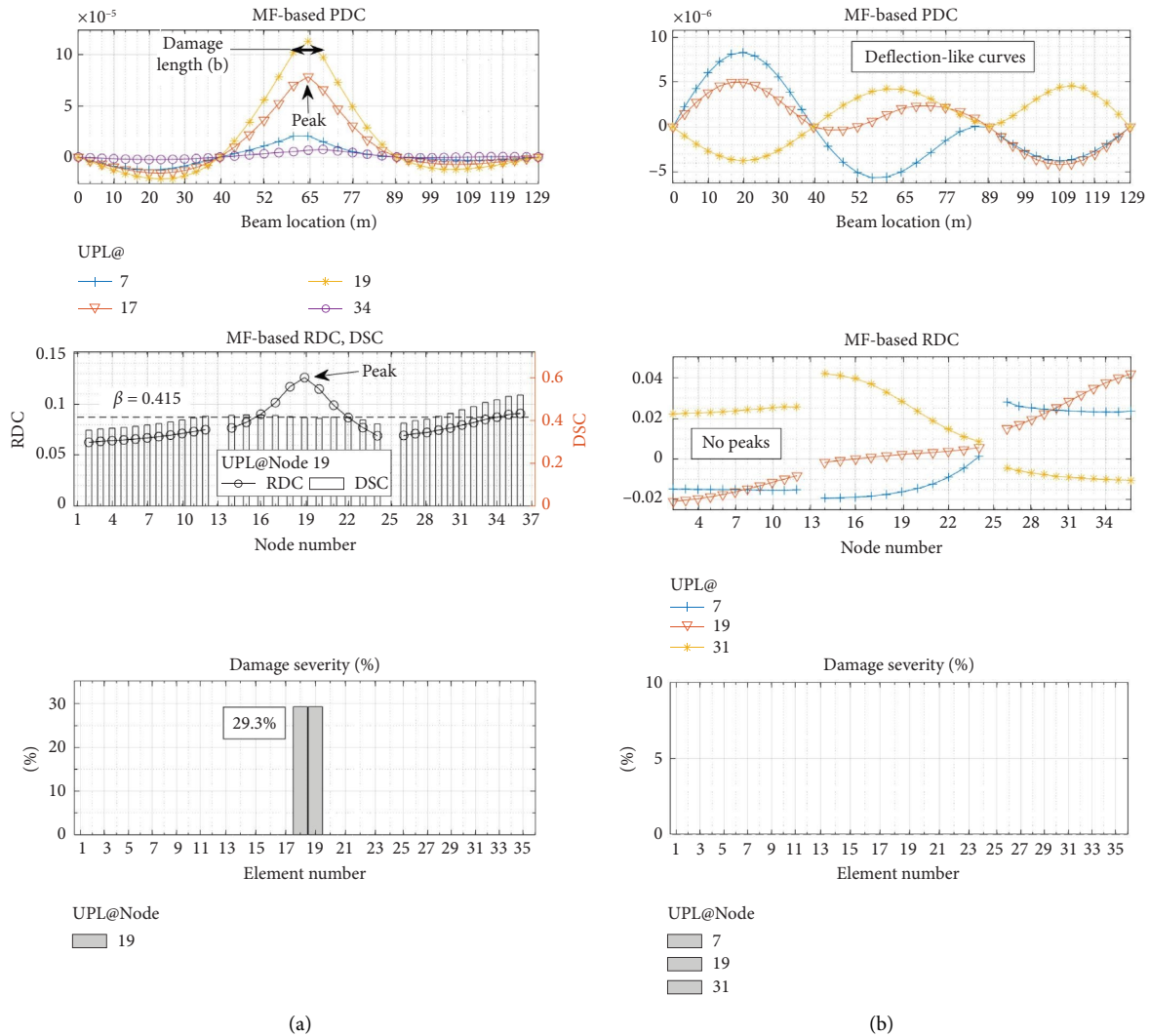
FIGURE 21: DI results of D2.1: (a) North girder; (b) South girder.

a peak appears at node No. 11 on the RDC plot under the UPL at node No. 31, but this peak is absent on the other two RDC plots. Therefore, further investigation is needed to determine the extent of the damage and confirm whether all three peaks are caused by real damage.

First, assume that all the three peaks are subjected to damage. Consider three damaged regions occurred on the girder at elements No. 10-11, No. 18-19 and No. 30-31. By gradually assigning these damaged regions to the SSVB model, the reference $RDC_i^{50\%}$ ($i = 1,2,3$) were computed. On substitution and solving equations (30) and (31) (similar to solving damage case D1.2 in Section 3), the damage severities of the three damaged regions are determined and shown in Figures 24(a3). Results indicate that the suspected damage at beam elements No. 10-11 and 30-31 is not obvious and can be discarded since by nature the damage severity could not be greater than 100% or below zero percent. Therefore, damage quantification result of the first trail would lead to the rejection of damage at the first and the third damage at beam elements No. 10-11 and 30-31.

For the second trail, only a single damaged region at elements No. 18-19 is considered. Figures 24(b1), 24(b2) and 24(b3) show the DI result using MF-based proportional deflections under the UPL at node 19, which is closest to the damage element. The corresponding damage quantification results are $\beta = 1.76$ and $\alpha = 63.7\%$, which is around 5% error compared to previous numerical investigation result of $\alpha = 67.2\%$ for the damage case D2-4 in Figure 23(a).

It is evidenced from the above analyses that the proposed DI method has the capacity to reject false positive detections that are common in practice, especially in large-scale structures, where measurement noise is unavoidable.

The treatment of measurement noise data is next investigated. The ovals in Figure 24(b1) and 24(b2) mark the positions of sensors N2 and N4 in the field test (Figure 12), which present abnormal changes that are not relevant to theoretical damage-induced patterns on the PDC and RDC plots. It appears that high measurement noise was present in these sensors, and this resulted in the unusual fluctuation and low range of the damage severity consistency DSC plot
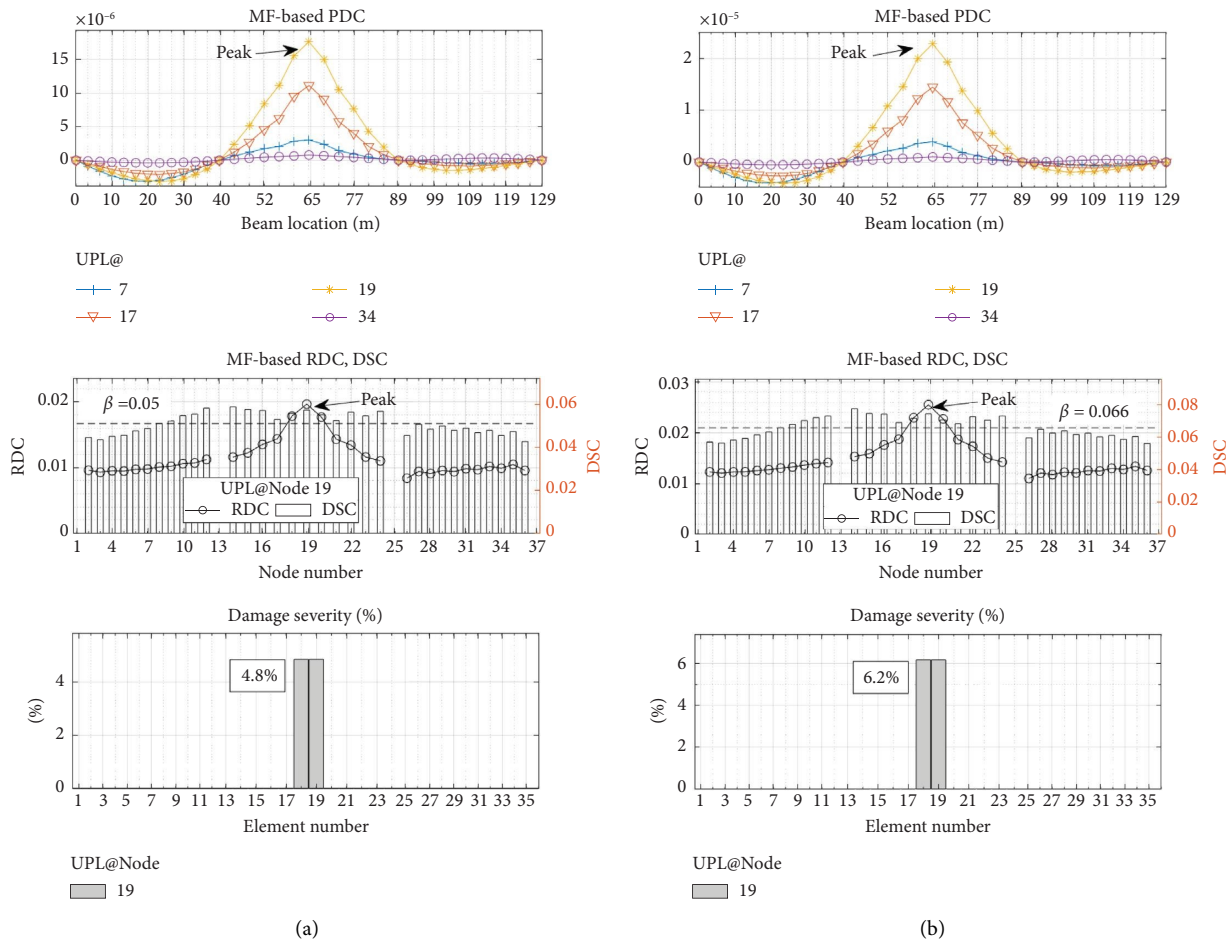
Figure 22: DI results for North girder: (a) D2.2; (b) D2.3.

on the third span compared to other spans as shown in Figure 24(b2). To improve the damage detection results, high noisy sensors N2 and N4 are removed, and the corresponding mode shape displacements at these sensors are interpolated from the remaining sensors using the shape-preserving piecewise cubic interpolation. The subsequent damage detection results are presented in Figure 25(a). Compared to Figure 24(b), the noisy data removal only improves the result on the third span and does not affect the original PDC, RDC and DSC plots at the remaining sensor locations including the middle node of third span and the entire first and second spans. With a more consistent DSC function, the damage severity is recalculated as $\alpha = 66.2\%$, which approximates numerical result of 67.2% in Figure 23(a), with only 1.5% error (Table 10).

Finally, it is of great interest to investigate the accuracy of the proposed method using fewer modes of vibration. Figure 25(b) presents the damage assessment results when only the first 5 modes are used, which provides less consistent DSC plot, yet satisfactory damage quantification results of 62.3% compared to numerical result of 67.2% using all six modes. Figures 26(a) and 26(b) present the results when only flexural modes are considered. It is evidenced that while the damage locating criteria are clear on the plots, the

damage severity was overestimated with 24.4% and 26.6% errors compared to those obtained numerically using six modes (Table 10). Table 10 presents other DI results when different number of modes are used. It is evident that the second mode (torsional mode) could not be discarded in this case study, and that at least the first two or three modes should be considered to have accurate damage quantification results.

In summary, numerical and experimental verifications of the benchmark I-40 girder bridge demonstrated that the proposed DBDI method can accurately locate and quantify different damage scenarios in complex structures. In addition, the method can eliminate false positive damage detection due to measurement noise, which is unavoidable in practice.

5. Experimental Validation on a Large-Scale BGB

5.1. Test Description. To demonstrate the applicability of the proposed method to statically determinate beams, further experimental validation was carried out on a large-scale single-span BGB model as shown in Figure 27. The tested model is a 6-m-long simply supported reinforced concrete
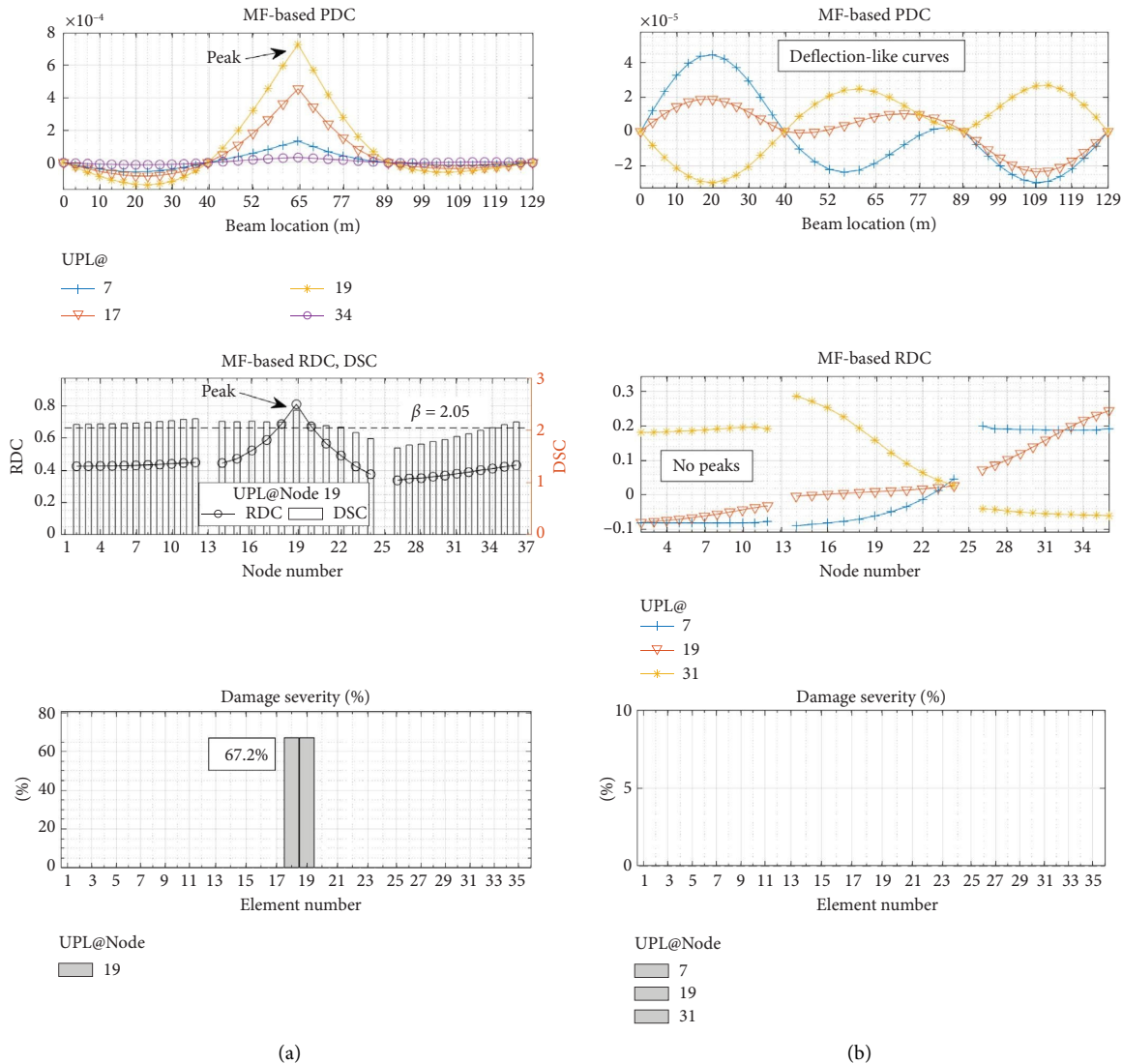
FIGURE 23: DI results for D2.4: (a) North girder; (b) South girder.

single box girder, with a support-to-support span of 5.8 m. The test model was constructed at the Queensland University of Technology for various SHM research topics [47, 48], including DI in large-scale girder bridges in the present paper. The basic dimensions of the model are given in Figure 28.

The data acquisition system includes 17 lightweight 8630B5 Kistler piezoelectric accelerometers having 1 V/g sensitivity, ±5 g input range and a broad frequency response range of 0.5–2000 Hz. It also includes an NI cDAQ-9172 chassis and six NI-9234 bridge modules to form up to 24 single-axis accelerometer measurement channels. Among various sensor layouts used during the test, the layout with sensors mounted along the central line of the bottom and top flanges is used in this study (Figure 28). The transducers were used to measure the BGB vertical acceleration at the sampling rate of 2048 Hz. An in-house LabVIEW professional app was used to read and log the data in a fully synchronised and automated acquisition manner [49].

Vibration tests were conducted to capture the modal parameters of the intact structure before two damage states were created. The first damage state, denoted in this paper as D3.1, was formed under cyclic loads from a MOOG (manufactured by Moog Inc.) test system placed at midspan of the BGB (Figure 27). Six cracks named as CR2 to CR7 occurred at the bottom flange and lower part of the webs within ±0.5 m from the middle span in this damage scenario (Figure 29). The second damage state, denoted as D3.2, was later created by applying further static loads in the same position. As a result, two more cracks named CR1 and CR8 were found at approximately ±1 m from the midspan, while the previous six cracks opened and propagated further to the upper part of the webs but did not reach the top flange (Figure 29). Therefore, the visible damage length for damage case D3.1 is 1 m and 2 m for the second damage case D3.2.

In each damage state, the MOOG was lifted from the girder for free vibration tests. Vibration signals of the BGB were recorded under random hammer excitation using the
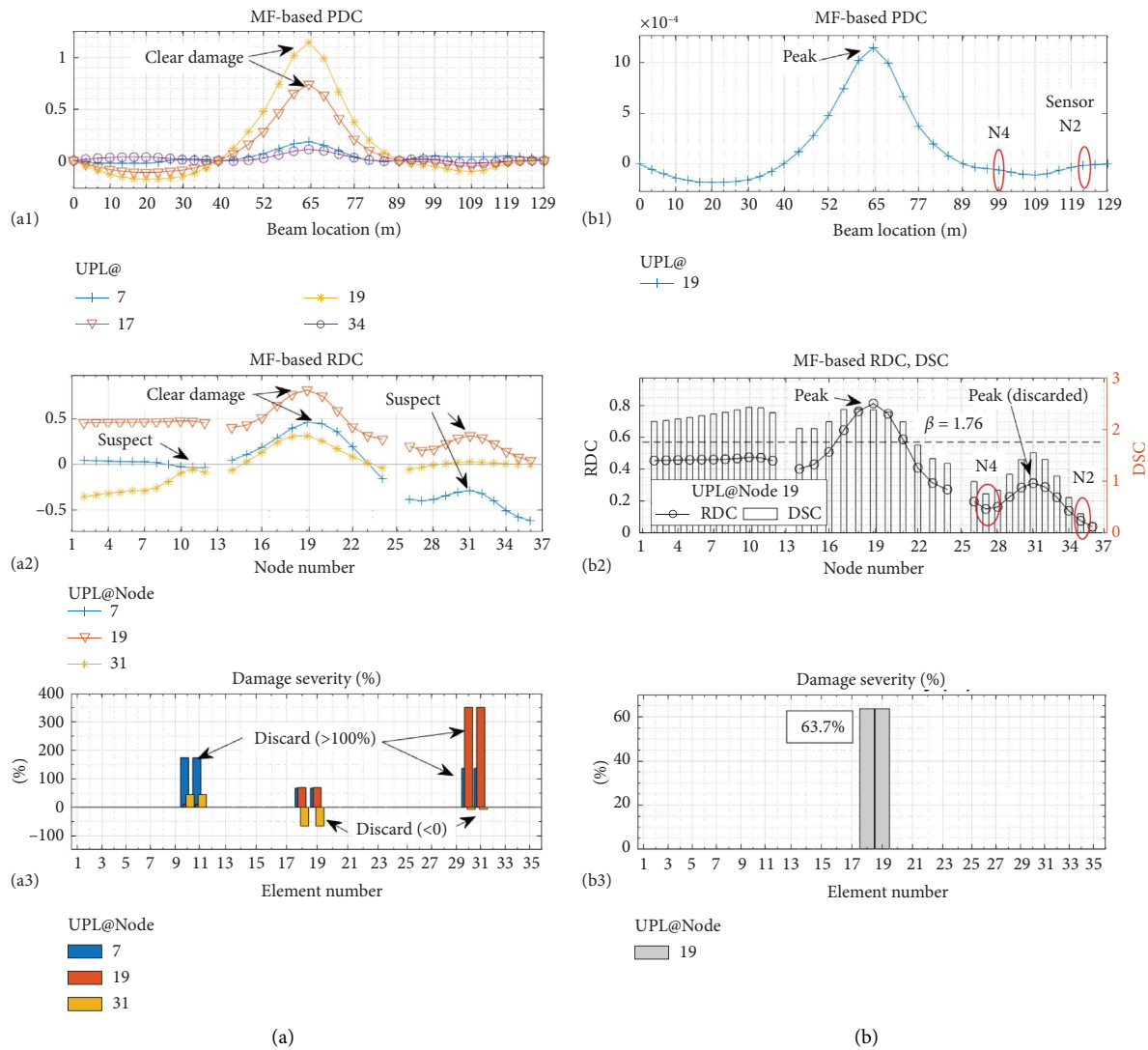
FIGURE 24: Experimental DI results for E-4: (a) first trial—three damages; (b) second trial—one damage.

data acquisition system. Modal parameters were then estimated using the enhanced frequency-domain decomposition (EFDD) method from the OMA software ARTeMIS [50]. A typical modal estimation plot is presented in Figure 30. The identified natural frequencies before and after the two damage states are summarised in Table 11, which shows a clear reduction trend associated with the progressive damage introduced to the BGB. It should be noted that modal parameters reported in this paper can be different from those reported elsewhere due to different testing conditions, mostly due to boundary changes after each test rearrangement for different SHM research topics. Figure 31 illustrates the first three of the identified mode shapes, of which the first is in pure bending, while the other two are coupled modes with the bending response generally being dominant. Obtaining higher-order pure bending modes was challenging in this situation probably due to the limitation in bandwidth of the manual excitation method used in this case.

To serve as input data for DI, the identified unit mode shapes extracted from accelerometers mounted under the bottom flange were interpolated into 13 output points at a spacing of 400 mm and 500 mm (Figure 28) using the shape-preserving piecewise cubic interpolation method. Construction of the PMF matrices and extraction of the proportional deflections were performed subsequently to create input data for DI in the next section.

5.2. DI Results. Besides confirming the presence and location of the damage on the BGB, the main focus of this case study is to test the SSVB concept in quantifying the damage in statically determinate beams. Plots of DI results for the two scenarios are presented in Figures 32(a) and 32(b). Similar to the previous case studies, the damage location can be identified within the middle region of the box girder corresponding to the peak region on the MF-based PDCs and RDCs. The damage location is also confirmed by the increasing trend in the peak's magnitude when the UPL is
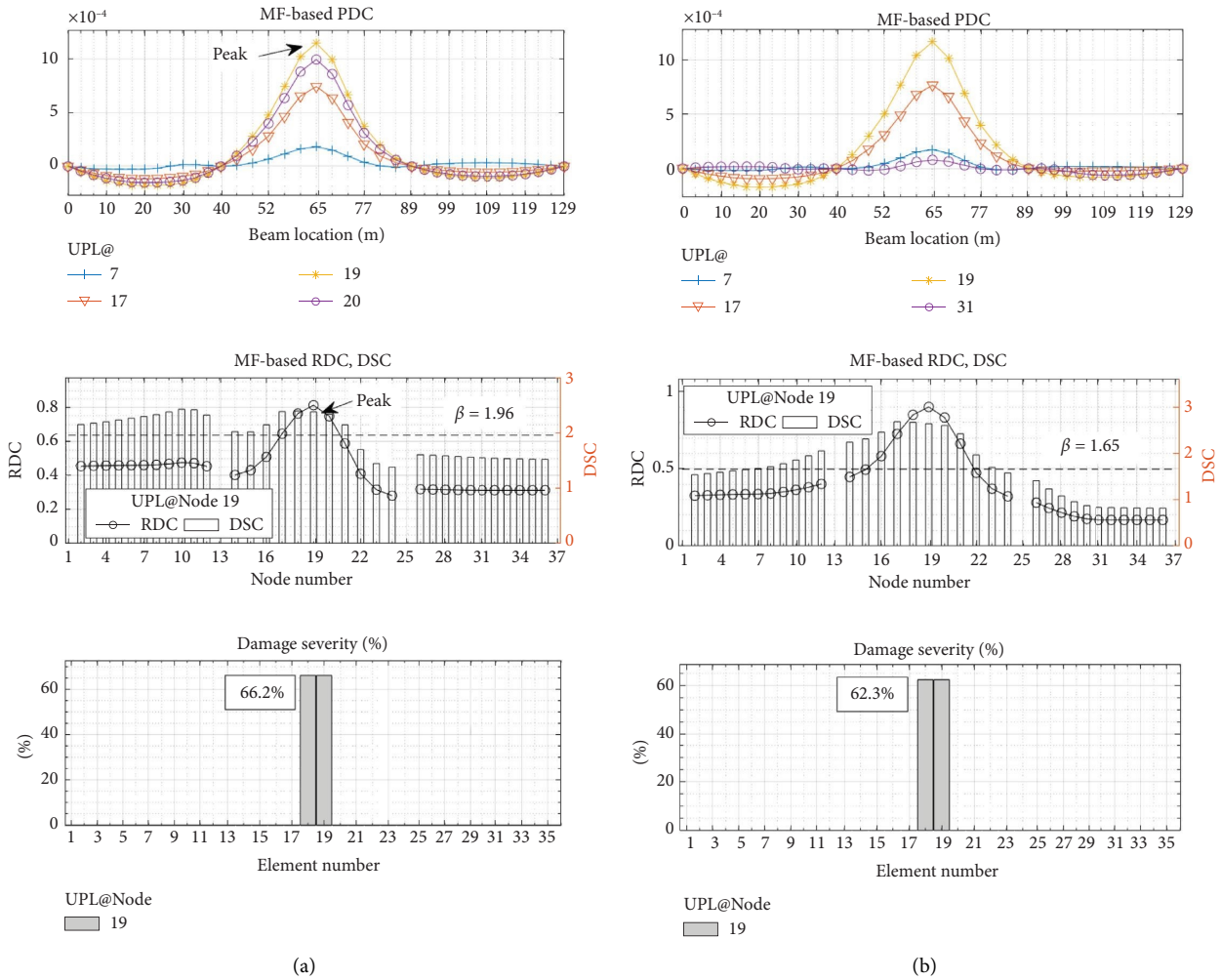
FIGURE 25: DI results for E-4 after removing high-noise sensors: (a) using all 6 modes; (b) using first five modes.

TABLE 10: Damage identification results using different number of modes (damage case E-4).

Modes used	Damage located	Damage extent (%)	Error (%) compared to numerical study[*]
First 6 modes	Yes	66.2	−1.5
First 5 modes	Yes	62.3	−7.3
First 4 modes	Yes	62.3	−7.3
First 3 modes	Yes	63.7	−5.2
First 2 modes	Yes	63.6	−5.4
First flexural mode	Yes	83.60	24.4
First three flexural modes	Yes	85.1	26.6

[*]Numerical study using 6 modes presented in Figure 23.

moved closer to node No. 7 at midspan (Figure 32, first row). The MF-based DSC function on the second row of Figure 32 indicates that the less severe damage case D3.1 is more affected by measurement noise (with higher DSC variations) compared to the more significant damage case D3.2 (satisfactory constant DSC).

Once the presence of damage and its location were confirmed, the SSVB method was used to estimate the damage severities over the known 1m-long girder portion for D3.1 and 2m-long for D3.2 (Figure 29). A simple 5.8-m-long simply supported SSVB model was created, with arbitrarily constant cross section (Figure 33(a)). Two virtual 50% damage scenarios were then assigned to the SSVB (Figures 33(b) and 33(c)) and the MF-based deflections were used to calculate the $RDC^{50\%}$ for the two damage scenarios. As a result, the damage severities were estimated as 19.7% and 32.1% for D3.1 and D3.2, respectively (Figure 33—last row). Numerical simulations on a BGB FE model (Figure 34) later confirmed that the amount of 19.7% and 32.1% of damage assigned to the model resulted in approximate
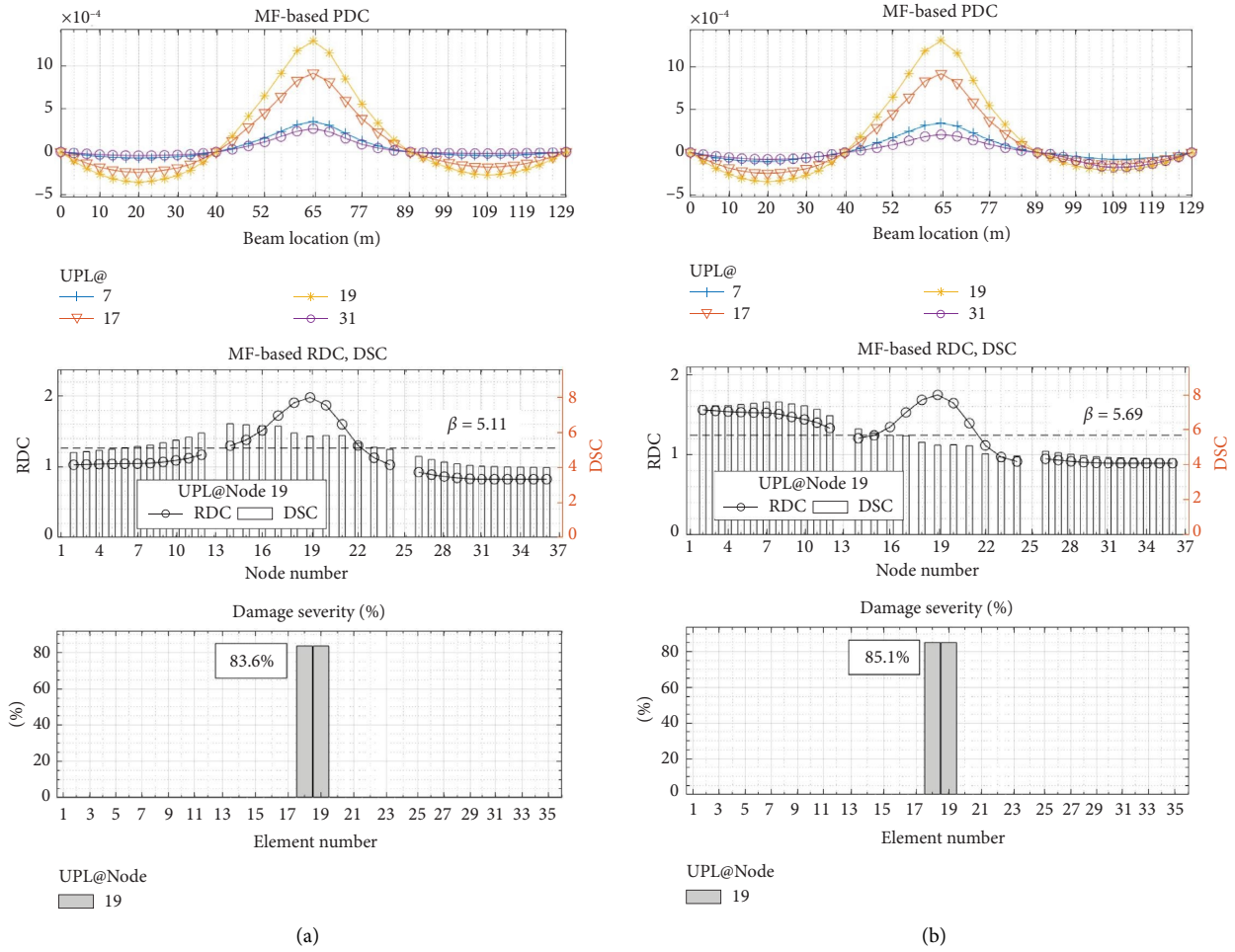
FIGURE 26: DI results using flexural modes only: (a) using first flexural mode; (b) using flexural modes 1, 3, 4.
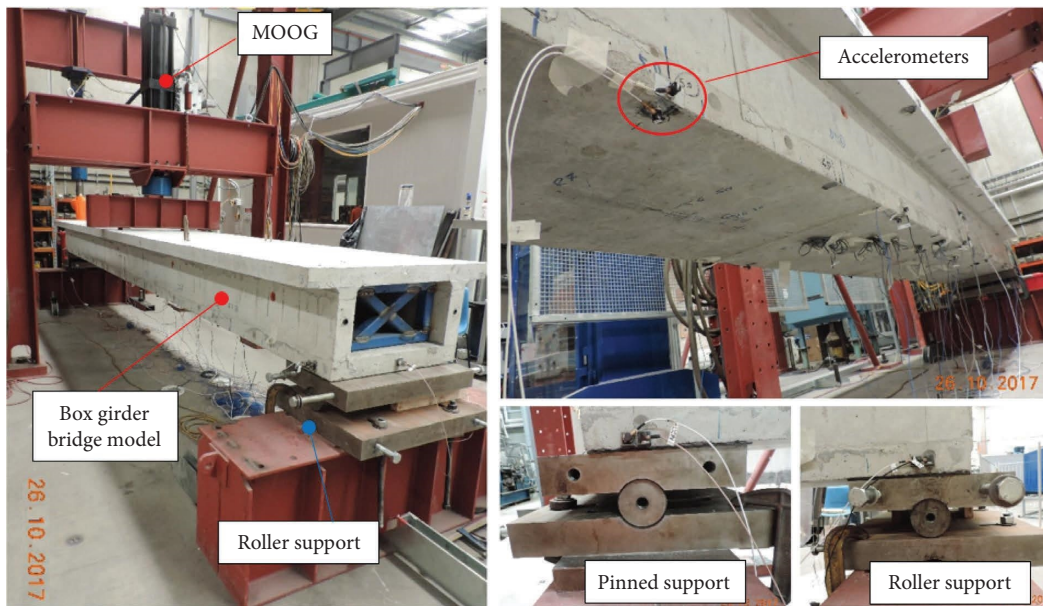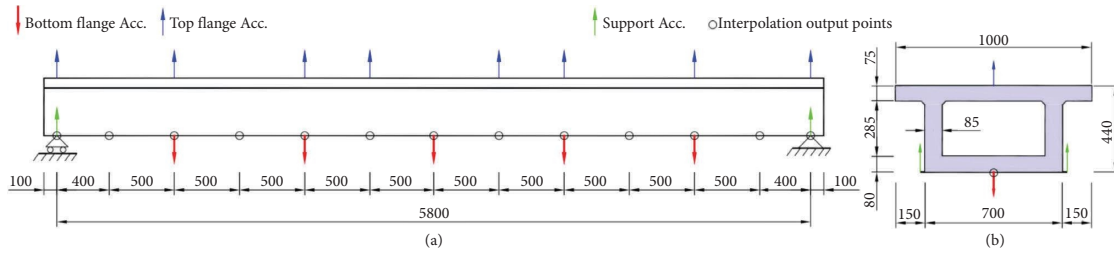

FIGURE 27: The BGB test setup.

FIGURE 28: Schematic diagram of the test model: (a) side view; (b) cross section (length in mm; Acc. = accelerometers) (girder dimensions are taken from Pathirage [48]).
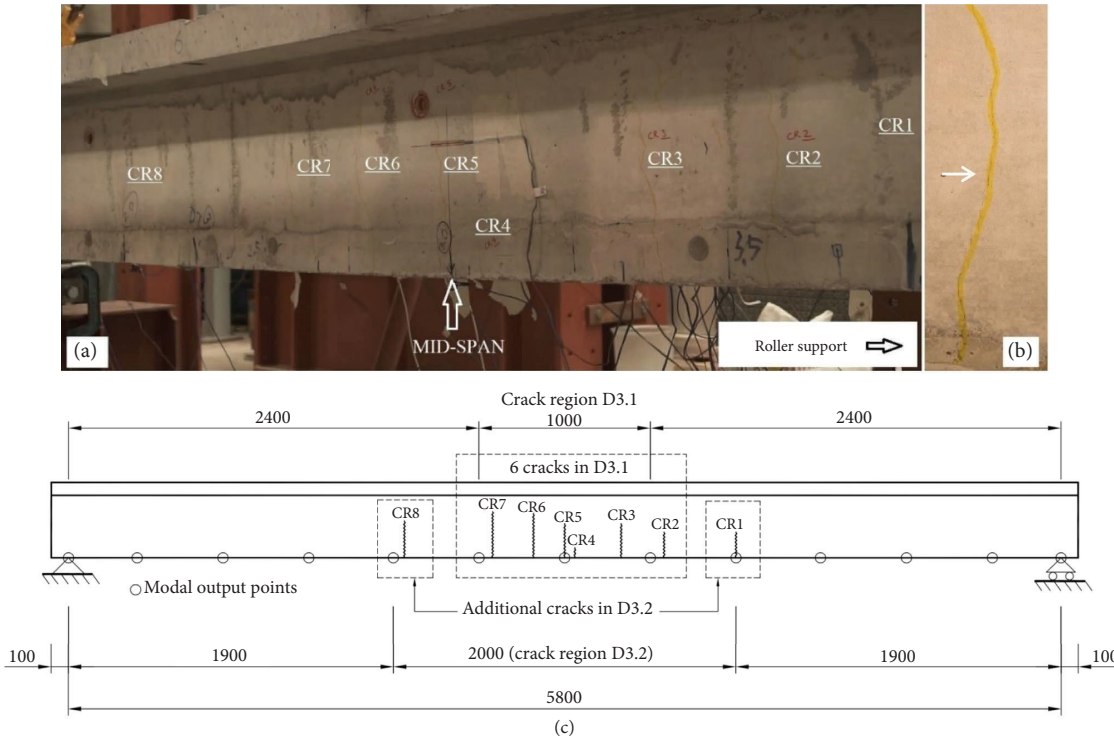

FIGURE 29: (a) Crack arrangements in D3.2. (b) A typical crack in D3.2 damage state. (c) Crack range schematic.
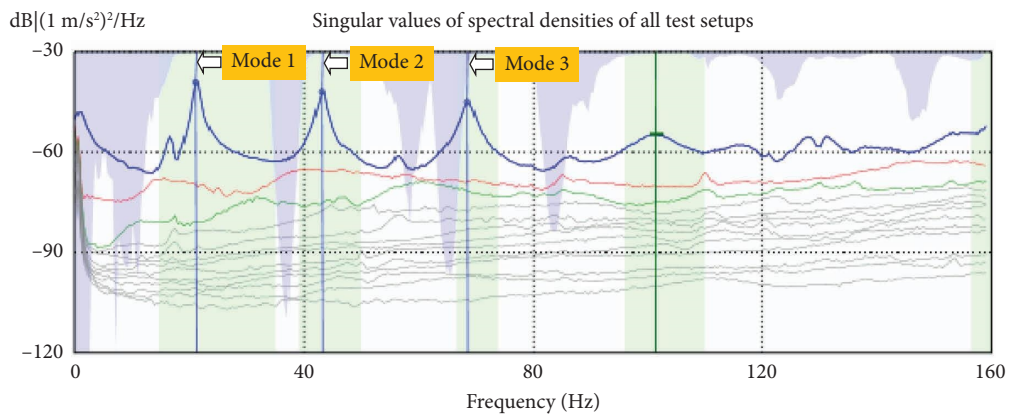

FIGURE 30: A typical modal estimation plot of the BGB model using EFDD method.

frequencies compared to experiment results, with less than 1% relative difference (last row of Table 12). Furthermore, the relative changes of 3.7% and 11.5% of the fundamental

frequency in the two simulated damage scenarios compared to the intact state (second last row of Table 12) are close to the corresponding reductions of 4.4% and 10.6% (Table 11)

TABLE 11: Natural frequencies for the intact and the damaged beam.

Mode	Intact	D3.1	D3.2	Note
1	21.22	20.29 (−4.4%)	18.97 (−10.6%)	First bending mode
2	43.17	41.73 (−3.3%)	41.07 (−4.9%)	Coupled mode – bending dominant
3	68.61	67.30 (−1.9%)	62.30 (−9.2%)	Coupled mode – bending dominant

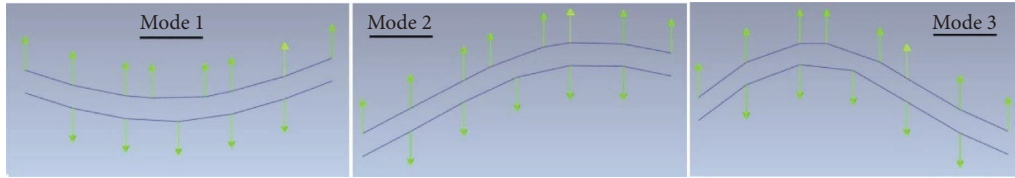Note: Values within (...) are relative changes compared to the intact state.

FIGURE 31: Identified mode shapes of the intact BGB model (left end: roller support).
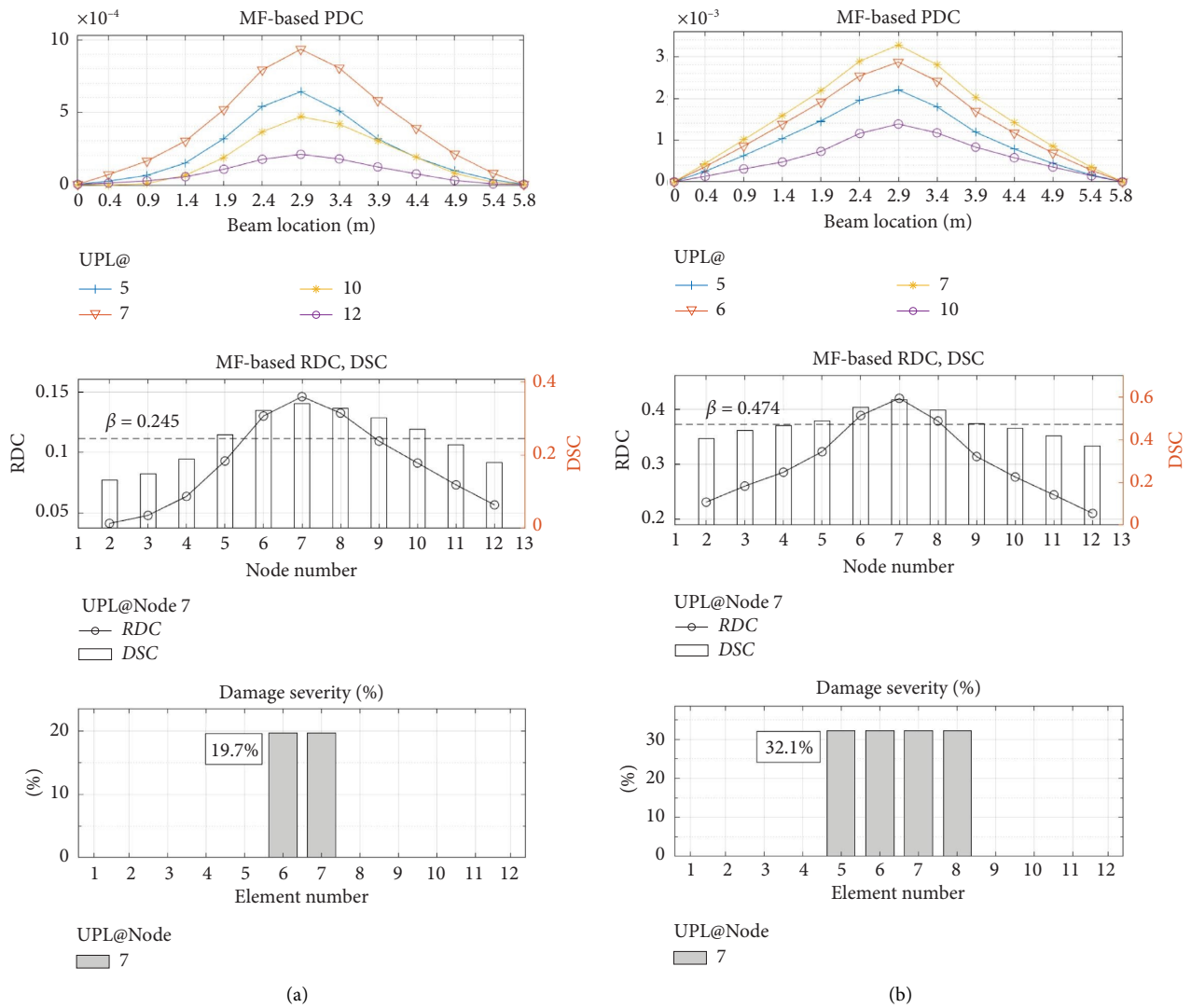
FIGURE 32: Damage quantification result: (a) D3.1; (b) D3.2.

observed in the experiment. Better agreements could have been achieved if more pure bending modes had been obtained from the experiment and used to quantify the damage. Nevertheless, it is evident that the DI method for continuous beams incorporated with the SSVB method proposed in this paper is also applicable to statically
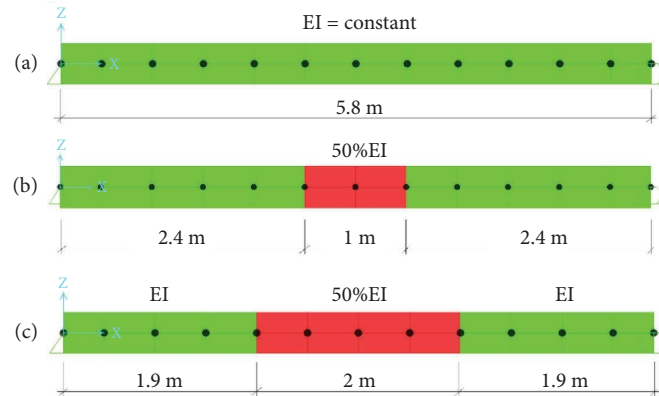
FIGURE 33: The SSVB of the BGB models: (a) undamaged; (b) virtual damage D3.1; (c) virtual damage D3.2.
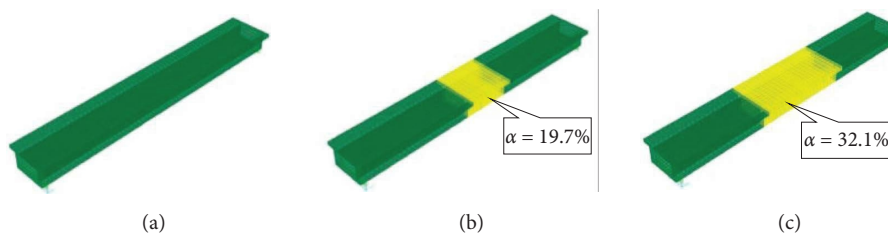

FIGURE 34: Numerical simulation of the BGB: (a) intact; (b) D3.1; (c) D3.2.

TABLE 12: FE validation of the damage quantification results for the BGB.

Parameter	Intact	D3.1	D3.2	Note
Damage severity	0%	19.7%	32.1%	
ρ (kg/m^3)	2500	2500	2500	
E (GPa)	22.5	18.07	15.28	At damaged elements
f_1 (Hz)	21.28	20.49 (−3.7%)	18.82 (−11.5%)	First bending mode (error compared to FE intact state)
Error (percentage change)	0.26%	0.99%	−0.79%	Compared to experimental f_1 results

determinate beams. One merit of the enhanced method is that it eliminates the need to calculate complicated scalar functions required in existing methods used in previous studies [4, 24].

6. Conclusions

This paper developed an enhanced deflection-based method for locating and quantifying damage in different beam-like structures, including single-span and multispan continuous girder bridges utilising either the changes in static deflections or output-only MF-based proportional deflections. The established general mathematical forms of damage-induced PDC and relative deflection change RDC functions provide patterns that can reveal the damaged and undamaged beam spans, as well as the damage location(s). A new damage quantification method using an SSVB concept was proposed. Key achievements in this paper include the following:

- Mathematical damage-induced PDC and RDC formulae successfully developed for multispan beams, also applicable to statically determinate beams.

- Introduction of additional damage-locating criteria to distinguish the undamaged spans from the damaged ones and precisely locate damage within affected spans.

- Establishment of the SSVB concept for damage quantification, applicable to any type of Euler–Bernoulli beam (unlike previous formula-based methods limited to simply supported or cantilever beams).

The proposed method's performance was initially validated through a numerical simulation on a double-span beam model, subjected to both single and multiple damage scenarios. The feature plots were shown to accurately represent damage-induced patterns pertinent to the proposed multiple damage location criteria. Following the successful location of the damage, the damage severity was correctly estimated. The method was further validated both numerically and experimentally on a real bridge, the benchmark I-40. The results demonstrated the method's ability to accurately identify and quantify damage. In numerical simulations, the damage quantification error was proved negligible through verifications on known damage severity scenarios. In experimental verifications, when using all six modes, the error compared to

the numerical simulation remained minor (less than 2%). Even with a smaller number of multiple modes adopted, the error remains below eight percent reflecting a desired performance. Notably, the method remained robust against false positive detections caused by measurement noise, providing accurate damage location and severity estimates. All these illustrate the outstanding performance of the proposed method in identifying and quantifying damage of this well-known but challenging benchmark bridge.

The capacity of the method was further demonstrated through an additional experimental verification on a large-scale BGB model, showcasing its relevance to statically determinate beams. The results indicated that this enhanced method can be utilised to quantify damage in statically determinate beams, eliminating the need to calculate the scalar functions as required by existing methods. Ultimately, these verification results showed that the developed method has the potential to be a reliable and versatile tool for the DI of many highway bridges.

Future research could explore the application and extension of the proposed method to other types of structures beyond Euler–Bernoulli beam–like configurations. Additionally, integrating the SSVB concept with alternative measurement parameters, other than flexural deflections, can enhance damage assessment along the beam and near the supports. Lastly, leveraging advanced sensor technologies and machine learning algorithms could further enhance the accuracy and efficiency of damage detection and quantification in large-scale bridge systems.

Appendix A. FE Illustration of Relative Bending Moment Change Coefficient

To validate the approximation in equation (8) (Section 2.1.2), a FE analysis was carried out on a two-span beam with a 20% damage severity (80% stiffness remaining) in a 10% segment of the second beam span (Figure A1). Under the point load of 100 kN acting at node 7 on the first span, changes in the bending moments at different beam positions are illustrated in Figure A1 and summarised in Table A1. As expected by the explanations in Section 2.1.2, the relative bending moment change $\zeta_M(x_2, x_L)$ consistently remained at 0.0086 on the second span (without load applied). On the first span, where the point load was applied, $\zeta_M(x_1, x_L)$ exhibited some variation, ranging from 0.0022 to 0.0104. However, when these values were added to 1, the variation became negligible, as illustrated in Figure A2. This supports the approximation made in equation (8), which is crucial for the DI method presented in this study.
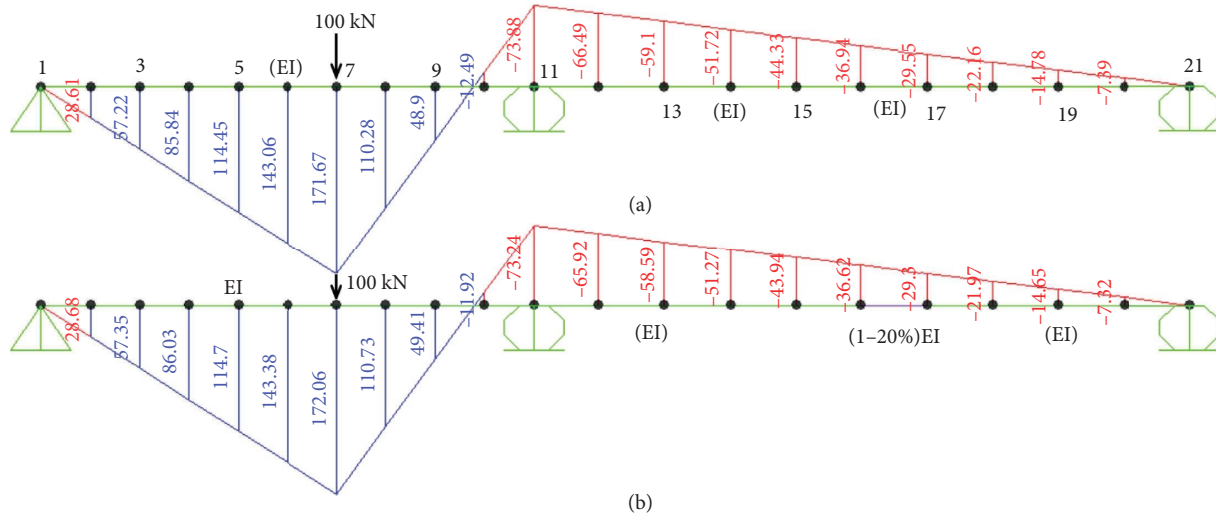

FIGURE A1: Illustration of moment changes due to damage: (a) undamaged state (M^h); (b) damaged state (M^d).

TABLE A1: Illustration of the relative bending moment change coefficients.

Span	1st span				2nd span				
Node No.	3	5	7	9	11	13	15	17	19
M^h (kNm)	57.224	114.448	171.672	48.896	−73.880	−59.104	−44.328	−29.552	−14.776
M^d (kNm)	57.352	114.704	172.055	49.407	−73.241	−58.593	−43.945	−29.297	−14.648
$\Delta M = M^d \text{-} M^h$	0.1278	0.2554	0.3832	0.5109	0.6386	0.5109	0.3832	0.2554	0.1278
$\zeta_M (x_1, x_L)$	0.0022	0.0022	0.0022	0.0104	0.0086	0.0086	0.0086	0.0086	0.0086
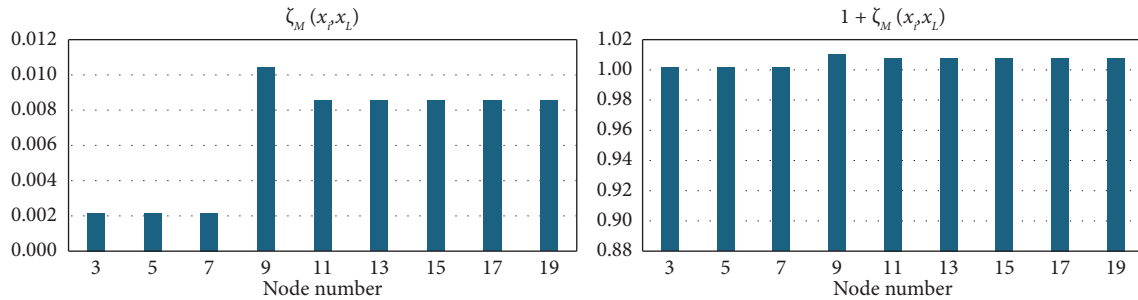
FIGURE A2: Variation of $\zeta_M (x_i, x_L)$ and $1 + \zeta_M (x_i, x_L)$ along the beam.

Data Availability Statement

The data used to support the findings of this study are available from the corresponding author upon request.

Disclosure

This paper originates from a study on structural health monitoring of civil structures at the Queensland University of Technology (QUT), Australia [5].

Conflicts of Interest

The authors declare no conflicts of interest.

References

[1] A. Zingoni, "Structural Health Monitoring, Damage Detection and Long-Term Performance," *Engineering Structures* 27, no. 12 (2005): 1713–1714, https://doi.org/10.1016/j.engstruct.2005.06.001.

[2] T. H. T. Chan and D. P. Thambiratnam, *Structural Health Monitoring in Australia* (Nova Science Publishers, 2011).

[3] S. W. Doebling, C. R. Farrar, and M. B. Prime, "A Summary Review of Vibration-Based Damage Identification Methods," *The Shock and Vibration Digest* 30, no. 2 (1998): 91–105, https://doi.org/10.1177/058310249803000201.

[4] N. T. Le, D. P. Thambiratnam, A. Nguyen, and T. H. T. Chan, "A New Method for Locating and Quantifying Damage in Beams from Static Deflection Changes," *Engineering Structures* 180 (2019): 779–792, https://doi.org/10.1016/j.engstruct.2018.11.071.

[5] N. T. Le, *Structural Damage Identification Using Static and Modal Flexibility-Based Deflections* (Queensland University of Technology, 2019).

[6] M. Sanayei and O. Onipede, "Damage Assessment of Structures Using Static Test Data," *AIAA Journal* 29, no. 7 (1991): 1174–1179, https://doi.org/10.2514/3.10720.

[7] M. R. Banan, M. R. Banan, and K. D. Hjelmstad, "Parameter Estimation of Structures from Static Response. I. Computational Aspects," *Journal of Structural Engineering* 120, no. 11 (1994): 3243–3258, https://doi.org/10.1061/(asce)0733-9445(1994)120:11(3243).

[8] M. R. Banan, M. R. Banan, and K. D. Hjelmstad, "Parameter Estimation of Structures from Static Response. II: Numerical Simulation Studies," *Journal of Structural Engineering* 120, no. 11 (1994): 3259–3283, https://doi.org/10.1061/(asce)0733-9445(1994)120:11(3259).

[9] K. D. Hjelmstad and S. Shin, "Damage Detection and Assessment of Structures from Static Response," *Journal of Engineering Mechanics* 123, no. 6 (1997): 568–576, https://doi.org/10.1061/(asce)0733-9399(1997)123:6(568).

[10] M. Sanayei, G. R. Imbaro, J. A. McClain, and L. C. Brown, "Structural Model Updating Using Experimental Static Measurements," *Journal of Structural Engineering* 123, no. 6 (1997): 792–798, https://doi.org/10.1061/(asce)0733-9445(1997)123:6(792).

[11] X. Wang, N. Hu, H. Fukunaga, and Z. Yao, "Structural Damage Identification Using Static Test Data and Changes in Frequencies," *Engineering Structures* 23, no. 6 (2001): 610–621, https://doi.org/10.1016/s0141-0296(00)00086-9.

[12] F. Bakhtiari-Nejad, A. Rahai, and A. Esfandiari, "A Structural Damage Detection Method Using Static Noisy Data," *Engineering Structures* 27, no. 12 (2005): 1784–1793, https://doi.org/10.1016/j.engstruct.2005.04.019.

[13] X.-Z. Chen, Z. Hong-Ping, and C. Chuan-Yao, "Structural Damage Identification Using Test Static Data Based on Grey System Theory," *Journal of Zhejiang University - Science* 6, no. 8 (2005): 790–796, https://doi.org/10.1631/jzus.2005.a0790.

[14] Q. Yang and B. Sun, "Structural Damage Localization and Quantification Using Static Test Data," *Structural Health Monitoring* 10, no. 4 (2011): 381–389, https://doi.org/10.1177/1475921710379517.

[15] S. S. Kourehli, A. Bagheri, G. G. Amiri, and M. Ghafory-Ashtiany, "Structural Damage Detection Using Incomplete Modal Data and Incomplete Static Response," *KSCE Journal of Civil Engineering* 17, no. 1 (2013): 216–223, https://doi.org/10.1007/s12205-012-1864-2.

[16] I. Š. Grandić and D. Grandić, "Estimation of Damage Severity Using Sparse Static Measurement," *Journal of Civil Engineering and Management* 23, no. 2 (2017): 213–221.

[17] I.-Y. Choi, J. S. Lee, E. Choi, and H.-N. Cho, "Development of Elastic Damage Load Theorem for Damage Detection in a Statically Determinate Beam," *Computers & Structures* 82, no. 29-30 (2004): 2483–2492, https://doi.org/10.1016/j.compstruc.2004.07.003.

[18] M. A.-B. Abdo, "Parametric Study of Using Only Static Response in Structural Damage Detection," *Engineering Structures* 34 (2012): 124–131, https://doi.org/10.1016/j.engstruct.2011.09.027.

[19] K. Koo, S. Sung, J. Park, and H. Jung, "Damage Detection of Shear Buildings Using Deflections Obtained by Modal Flexibility," *Smart Materials and Structures* 19, no. 11 (2010): 115026, https://doi.org/10.1088/0964-1726/19/11/115026.

[20] K. Koo, S.-H. Sung, and H.-J. Jung, "Damage Quantification of Shear Buildings Using Deflections Obtained by Modal Flexibility," *Smart Materials and Structures* 20, no. 4 (2011): 045010, https://doi.org/10.1088/0964-1726/20/4/045010.

[21] S. Sung, K. Koo, H. Jung, and H. Jung, "Damage-induced Deflection Approach for Damage Localization and Quantification of Shear Buildings: Validation on a Full-Scale Shear Building," *Smart Materials and Structures* 21, no. 11 (2012): 115013, https://doi.org/10.1088/0964-1726/21/11/115013.

[22] K. Y. Koo, J. J. Lee, C. B. Yun, and J. T. Kim, "Damage Detection in Beam-like Structures Using Deflections Obtained by Modal Flexibility Matrices," *Smart Structures and Systems* 4, no. 5 (2008): 605–628, https://doi.org/10.12989/sss.2008.4.5.605.

[23] T. Toksoy and A. Aktan, "Bridge-condition Assessment by Modal Flexibility," *Experimental Mechanics* 34, no. 3 (1994): 271–278, https://doi.org/10.1007/bf02319765.

[24] N. T. Le, A. Nguyen, D. Thambiratnam, T. Chan, and T. Khuc, "Locating and Quantifying Damage in Beam-like Structures Using Modal Flexibility-Based Deflection Changes," *International Journal of Structural Stability and Dynamics* 20, no. 10 (2020): 2042008, https://doi.org/10.1142/s0219455420420080.

[25] G. Bernagozzi, C. Ventura, S. Allahdadian, Y. Kaya, L. Landi, and P. Diotallevi, "Application of Modal Flexibility-Based Deflections for Damage Diagnosis of a Steel Frame Structure," *Procedia Engineering* 199 (2017): 2026–2033, https://doi.org/10.1016/j.proeng.2017.09.468.

[26] G. Bernagozzi, S. Mukhopadhyay, R. Betti, L. Landi, and P. P. Diotallevi, "Output-only Damage Detection in Buildings Using Proportional Modal Flexibility-Based Deflections in Unknown Mass Scenarios," *Engineering Structures* 167 (2018): 549–566, https://doi.org/10.1016/j.engstruct.2018.04.036.

[27] G. Bernagozzi, S. Mukhopadhyay, R. Betti, L. Landi, and P. P. Diotallevi, "Proportional Flexibility-Based Damage Detection for Buildings in Unknown Mass Scenarios: The Case of Severely Truncated Modal Spaces," *Engineering Structures* 259 (2022): 114145, https://doi.org/10.1016/j.engstruct.2022.114145.

[28] S. W. Doebling and C. R. Farrar, "Computation of Structural Flexibility for Bridge Health Monitoring Using Ambient Modal Data," in *Proceedings of the 11th ASCE Engineering Mechanics Conference* (Lauderdale, FL, USA, 1996).

[29] R. Brincker and C. Ventura, *Introduction to Operational Modal Analysis* (John Wiley & Sons, 2015).

[30] M. Aenlle and R. Brincker, "Modal Scaling in Operational Modal Analysis Using a Finite Element Model," *International Journal of Mechanical Sciences* 76 (2013): 86–101, https://doi.org/10.1016/j.ijmecsci.2013.09.003.

[31] Y. Ni, H. Zhou, K. Chan, and J. Ko, "Modal Flexibility Analysis of Cable-Stayed Ting Kau Bridge for Damage Identification," *Computer-Aided Civil and Infrastructure Engineering* 23, no. 3 (2008): 223–236, https://doi.org/10.1111/j.1467-8667.2008.00521.x.

[32] D. Bernal and B. Gunes, "Damage Localization in Output-Only Systems: A Flexibility Based Approach," in *Proc. Of the International Modal Analysis Conference (IMAC) XX* (2002).

[33] D. Bernal and B. Gunes, "Flexibility Based Approach for Damage Characterization: Benchmark Application," *Journal of Engineering Mechanics* 130, no. 1 (2004): 61–70, https://doi.org/10.1061/(asce)0733-9399(2004)130:1(61).

[34] Z. Duan, G. Yan, J. Ou, and B. F. Spencer, "Damage Detection in Ambient Vibration Using Proportional Flexibility Matrix with Incomplete Measured DOFs," *Structural Control and Health Monitoring* 14, no. 2 (2007): 186–196, https://doi.org/10.1002/stc.149.

[35] Z. Duan, G. Yan, J. Ou, and B. Spencer, "Damage Localization in Ambient Vibration by Constructing Proportional Flexibility Matrix," *Journal of Sound and Vibration* 284, no. 1-2 (2005): 455–466, https://doi.org/10.1016/j.jsv.2004.06.046.

[36] A. Ghali, A. Neville, and T. G. Brown, *Structural Analysis: A Unified Classical and Matrix Approach* (CRC Press, 2014).

[37] W. Ford, *Numerical Linear Algebra with Applications: Using MATLAB* (Academic Press, 2014).

[38] A. K. Pandey and M. Biswas, "Damage Detection in Structures Using Changes in Flexibility," *Journal of Sound and Vibration* 169, no. 1 (1994): 3–17, https://doi.org/10.1006/jsvi.1994.1002.

[39] A. Berman and W. G. Flannelly, "Theory of Incomplete Models of Dynamic Structures," *AIAA Journal* 9, no. 8 (1971): 1481–1487, https://doi.org/10.2514/3.49950.

[40] J. Maeck and G. De Roeck, "Damage Assessment Using Vibration Analysis on the Z24-Bridge," *Mechanical Systems and Signal Processing* 17, no. 1 (2003): 133–142, https://doi.org/10.1006/mssp.2002.1550.

[41] C. R. Farrar, W. Baker, T. Bell, et al., "Dynamic Characterization and Damage Detection in the I-40 Bridge over the Rio Grande," *Los Alamos National Lab., NM (United States)* (1994).

[42] N. Stubbs, J.-T. Kim, and C. Farrar, "Field Verification of a Nondestructive Damage Localization and Severity Estimation Algorithm," in *Proceedings-SPIE the International Society for Optical Engineering* (Spie International Society for Optical, 1995).

[43] J.-T. Kim and N. Stubbs, "Nondestructive Crack Detection Algorithm for Full-Scale Bridges," *Journal of Structural*

Engineering 129, no. 10 (2003): 1358–1366, https://doi.org/10.1061/(asce)0733-9445(2003)129:10(1358).

[44] K.-D. Nguyen, T. H. T. Chan, and D. P. Thambiratnam, "Structural Damage Identification Based on Change in Geometric Modal Strain Energy–Eigenvalue Ratio," *Smart Materials and Structures* 25, no. 7 (2016): 075032, https://doi.org/10.1088/0964-1726/25/7/075032.

[45] S. Christides and A. Barr, "One-Dimensional Theory of Cracked Bernoulli-Euler Beams," *International Journal of Mechanical Sciences* 26, no. 11-12 (1984): 639–648, https://doi.org/10.1016/0020-7403(84)90017-1.

[46] J. K. Sinha, M. Friswell, and S. Edwards, "Simplified Models for the Location of Cracks in Beam Structures Using Measured Vibration Data," *Journal of Sound and Vibration* 251, no. 1 (2002): 13–38, https://doi.org/10.1006/jsvi.2001.3978.

[47] S. Jamali, T. H. T. Chan, A. Nguyen, and D. P. Thambiratnam, "Reliability-Based Load-Carrying Capacity Assessment of Bridges Using Structural Health Monitoring and Nonlinear Analysis," *Structural Health Monitoring* 18, no. 1 (2018): 20–34, https://doi.org/10.1177/1475921718808462.

[48] T. S. Pathirage, *Identification of Prestress Force in Prestressed Concrete Box Girder Bridges Using Vibration Based Techniques* (Queensland University of Technology, 2017).

[49] A. Nguyen, T. H. T. Chan, D. P. Thambiratnam, K. T. L. Kodikara, N. T. Le, and S. Jamali, "Output-only Modal Testing and Monitoring of Civil Engineering Structures: Instrumentation and Test Management," in *SHMII 2017 - 8th International Conference on Structural Health Monitoring of Intelligent Infrastructure, Proceedings* (2017).

[50] SVS, *SVS-ARTeMIS Extractor-Release 5.3* (2011).